



# The 23–24 March 2021 lava fountain at Mt Etna, Italy

Daniele Andronico<sup>1</sup> · Claudia D’Orlando<sup>2</sup> · Federica Pardini<sup>2</sup> · Alessandro La Spina<sup>1</sup> · Mattia de’ Michieli Vitturi<sup>2</sup> · Pietro Bonfanti<sup>1</sup> · Antonino Cristaldi<sup>1</sup> · Ferruccio Ferrari<sup>1</sup>

Received: 9 October 2023 / Accepted: 19 April 2024  
© The Author(s) 2024

## Abstract

In 2021, more than 50 paroxysmal episodes occurred at the South-East Crater (SEC) of Mt Etna, Italy. The 23–24 March lava fountain was one of the longest episodes and began with weak Strombolian explosions, gradually transitioning to lava fountaining. The eruption intensity then dropped more slowly than in previous episodes, resulting in pulsating Strombolian explosions dominated by ash emission. Thirty-four tephra samples were used to reconstruct the fallout dispersal and estimate the total erupted mass. Grain size, textural, petrological and geochemical analyses indicate different features and were compared with the gas phase (SO<sub>2</sub> and HCl) in the volcanic plume. By applying stochastic global optimization to simulations of the temporal evolution of the eruption column height and tephra dispersal and deposition, the total erupted mass retrieved ( $6.76 \times 10^8$  kg) matches well the total erupted mass estimation by the ground-based deposit ( $8.03 \pm 2.38 \times 10^8$  kg), reducing the column height throughout the episode from 6.44 to 4.5 km above sea level and resulting in a mass eruption rate ranging from  $1.96 \times 10^5$  to  $8.18 \times 10^3$  kg/s. The unusual duration of the March episode and the characteristics of the erupted products point to the change in explosive style and magma fragmentation from fountaining to ash emission phases, associated with a slower magma supply inducing a change in magma rheology and a final, prolonged ash generation. Furthermore, this study showed that using observational data and the variation in eruption source parameters for numerical simulations can improve the accuracy of predicting the dispersal plume, thus mitigating the potential impact of longer paroxysmal episodes.

**Keywords** Mt Etna · 23–24 March 2021 paroxysmal episode · Tephra fallout deposit · Eruption source parameters · Numerical modelling · HYSPLIT · PLUME · MoM-TSM

## Introduction

Among all the active basaltic volcanoes, Mt Etna, in Italy (Fig. 1), can probably boast of being the one characterized by the most intense and frequent explosive activity. This is one of the reasons why it is studied by researchers from all over the world, as well as so widely under continuous observation (and even visited very closely when it is erupting) by enthusiasts and tourists. Indeed, since 1995, Etna has generated more than 250 ‘paroxysmal episodes’ from

one of its summit craters, almost entirely in the course of sequences which typically last from weeks to a few months (Andronico et al. 2021a). In 2021 alone, in fact, more than 50 episodes occurred at the South-East Crater (SEC), the most active among the summit craters over the last 20 years. A first sequence of 17 paroxysms, regularly spaced over time, occurred from 16 February to 1 April, while another sequence of almost 40 episodes followed between 17 May and 23 October 2021, with frequency varying from 2 per day up to about 1 per month for the last two episodes (see INGV-OE Istituto Nazionale di Geofisica e Vulcanologia, Osservatorio Etneo—Sezione di Catania) weekly reports at <https://www.ct.ingv.it/index.php/monitoraggio-e-sorveglianza/prodotti-del-monitoraggio/bollettini-settimanali-multidisciplinari?limit=100&limitstart=200>; Musu et al. 2023). Remarkably, two more powerful lava fountains also occurred on 10 and 21 February 2022, respectively (INGV-OE 2022a, b).

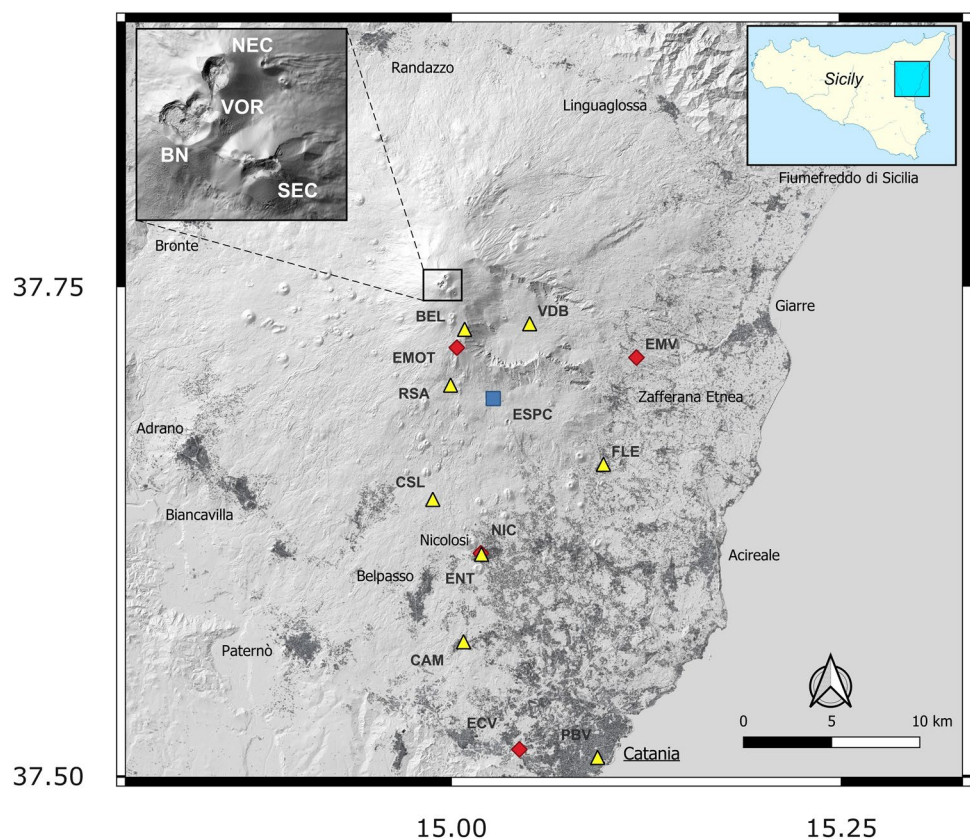
Editorial responsibility: S. Vergnolle

✉ Daniele Andronico  
daniele.andronico@ingv.it

<sup>1</sup> Istituto Nazionale di Geofisica e Vulcanologia - Osservatorio Etneo, Sezione di Catania, Catania, Italy

<sup>2</sup> Istituto Nazionale di Geofisica e Vulcanologia - Sezione di Pisa, Pisa, Italy

**Fig. 1** Map of Mt Etna with location of INGV-OE video cameras (full red diamonds) and seismic station used in this work (full blue square), and main sites reported in text (full yellow triangles). Camera labels: ECV, Cuad visible; EMOT, Montagnola thermal; EMV, Milo visible. Seismic station label: ESPC=Serra Pizzuta Calvarina. Main sites: BEL, Belvedere; CAM, Camporotondo; CSL, Chiesa S. Leo; FLE, Fleri; NIC, Nicolosi; PBV, Piazza Bovio; RSA, Rifugio Sapienza. Left inset: digital elevation model of the four summit craters in 2021: NEC, North-East Crater; VOR, Voragine; BN, Bocca Nuova; SEC, South-East Crater (modified from Proietti et al. 2023). Right inset: schematic map of Sicily (blue rectangle: map of Mt Etna)



Alparone et al. (2003) subdivided each paroxysmal episode into three eruptive phases, starting with a *resumption phase*, during which explosive activity resumes from a summit crater vent. An increase in terms of explosive frequency and intensity leads to the *paroxysmal phase*, characterized by strong Strombolian explosions and/or lava fountaining activity, typically accompanied by the rising of an eruption column above the crater and followed by the propagation of a volcanic cloud in the atmosphere which extends for tens to hundreds of km from the volcano (Andronico et al. 2021a and references therein). During each episode, a significant emission of lava flows usually occurs, with fluctuations in the effusive rate generally accompanying the waxing and waning trends of the explosive activity, respectively. A more or less rapid or gradual decline of both explosive and effusive phenomena finally characterizes the end of the paroxysmal episode (*conclusive phase*).

While the volcanic clouds can cause disruption in the atmosphere to air traffic, tephra fallouts can create problems for road traffic, due to the formation on the ground of variable thick and continuous deposits made up of ash and lapilli starting from the middle flanks of the volcano. Moreover, the effects of finer-grained particles on air quality in urban settlements constitute potential dangers to human health, especially in the case of wind-phenomena remobilization of volcanic ash with their subsequent suspension in the air

(Dominguez et al. 2020), which can affect the respiratory apparatus and irritate the eyes and skin (e.g. Horwell and Baxter 2006; Andronico and Del Carlo 2016), even interacting with anthropogenic pollutants causing the biological reactivity of organic compounds (Tomašek et al. 2021).

In addition to this episodic summit activity, two long-lasting explosive flank eruptions occurred in 2001 and 2002–2003 causing prolonged ash emission far away from Etna (Taddeucci et al. 2002; Andronico et al. 2008). Eventually, even minor explosive activities can still threaten the territory, with similar, albeit modest effects, especially on air traffic (Andronico et al. 2021a).

This high-frequent explosive activity makes Etna an extraordinary volcano for studying fallout deposits and erupted products in great detail (e.g. D’Orlando et al. 2022) and applying, testing and improving numerical models that simulate the ongoing explosive processes (Barsotti et al. 2010; Scollo et al. 2013; Spanu et al. 2016; Pardini et al. 2020). An example of where all these steps were followed is the tephra deposit emplaced on 23–24 March 2021, i.e. during the 16th episode of the first sequence in 2021, the second one in duration (more than 16 h). Unlike most of the previous 15 episodes, almost 6 h before the explosive activity completely ended, the sustained magma jets were replaced by pulsating low-intense Strombolian explosions accompanied and followed by continuous ash emission and

a significant reduction in the column height. At least 1 h before this change in eruptive style, the wind rotation from SSW to SE affected first the plume dispersal in the atmosphere and later the tephra fallout on the ground.

In the morning of 24 March, open-path Fourier transform infrared (OP-FTIR) solar occultation measurements of the gas phases were performed on the rotating volcanic cloud according to the sun's position. We also started to survey the SSW areas not yet affected by the fallout, completing our fieldwork on the SE slopes of Etna when the eruption had already stopped. Overall, we were able to map the tephra deposit and collect representative samples to reconstruct the tephra dispersal and estimate the main eruption source parameters: column height, total erupted mass, mass eruption rate and total grain size distribution. The finer-grained products (ash to fine lapilli particles) have also been studied for componentry, morphological and petrochemical analyses. In the following sections, we first present the chronology of the eruptive activity based on the observations from surveillance cameras located around the volcano, and correlate it with the pattern of the volcanic tremor. Both video and seismic signals are provided by the monitoring networks of INGV-OE, the main institution in charge of the volcanic and seismic monitoring in the eastern Sicily. Then, we describe the tephra fallout deposit and the eruption source parameters (in particular, total grain size distribution, total erupted mass and mass eruption rate) that we computed from field and observational data using standard methods, as the Voronoi tessellation (Bonadonna and Houghton 2005) and fitting curves of deposit thickness vs (area)<sup>1/2</sup> (Pyle 1989; Fierstein and Nathenson 1992; Bonadonna and Houghton 2005; Bonadonna and Costa 2012), and the textural and petrochemical features collected on the ash fraction of the erupted products. The temporal evolution of the height of the eruption column was retrieved by performing numerical simulations where the tephra transport and dispersal model Hybrid Single-Particle Lagrangian Integrated Trajectory (HYSPPLIT) (Stein et al. 2015) was applied to reproduce the observed deposit. To improve the characterization of the volcanic source, we initialized HYSPPLIT with the results of the eruption column model PLUME-MoM-TSM (de' Michieli Vitturi and Pardini 2021). A stochastic global optimization procedure was applied to numerical simulations to retrieve the values of column height (and their variation over time), which minimize the difference between the observed and simulated tephra ground deposit. Lastly, we discuss the volcanic pattern variability of paroxysmal episodes in terms of intensity and duration, focusing on how the change of explosive style from lava fountain to continuous ash emission affected tephra dispersal, mass loading per unit area and textural features of the erupted products during the 23–24 March episode, making its prediction very difficult and thus increasing its potential hazard on the territory.

## Methods

### Volcanic tremor

We analysed the tremor pattern as root-mean-square (RMS) amplitude expressed in m/s. The tremor was recorded by the INGV permanent seismic network at the summit station Etna Serra Pizzuta Calvarina (ESPC), a broadband (40-s cut-off period), three-component Trillium Nanometrics™ seismometer located at Serra Pizzuta Calvarina (latitude 37.6925, longitude 15.0274 and altitude 1655 m above sea level, hereafter a.s.l.; Fig. 1). The RMS amplitude values were calculated on the vertical component of ESPC in the band 0.5–5.5 Hz and averaged in 10-min-long windows (see Andronico et al. 2021a for more details on the formula used to calculate the root mean square). The amplitude of the tremor pattern is correlated to the evolution of the paroxysmal episode and can be crucial if unstable weather conditions prevent continuous observations of the eruptive activity (Alparone et al. 2003).

### OP-FTIR measurements

The SO<sub>2</sub>/HCl ratio, measured during daily surveys, was determined from solar occultation open-path Fourier transform infrared (FTIR) spectra. In this configuration, the gas plume is interposed between the sun (as infrared source) and the spectrometer (La Spina et al. 2023). Spectra were collected with a Midac spectrometer with a ZnSe beam splitter at 0.5 cm<sup>-1</sup> resolution. The detector is a Stirling-cooled mercury cadmium telluride (MCT) detector, sensitive between 500 and 5000 cm<sup>-1</sup>. The gas column amounts are retrieved using the forward model fitting techniques, described in Francis et al. (1998), between acquired and calculated spectrum, written in IDL language. The calculated spectrum is based on a radiative transfer model (available at <http://eodg.atm.ox.ac.uk/RFM/>) and the HITRAN molecular spectroscopic database (Rothman et al. 1998). The fitting procedure is calculated using the Rodgers (2000) equation with a Marquardt (1963) nonlinear iteration. For each solar spectrum, collected every 8 s, we retrieved the amounts (in units of molecules × cm<sup>-2</sup>) of SO<sub>2</sub> and HCl, the gas species with negligible concentrations in the free troposphere. This configuration prevents measurements of volcanic H<sub>2</sub>O and CO<sub>2</sub>, as the atmospheric components of paths through the entire atmosphere dominate the volcanic component of these species. The uncertainty on retrieved gas amounts is ~4%.

Linear regression of scatter plots of each species against SO<sub>2</sub> or HCl allows constraining their mean chemical ratios in the magmatic gas phases (Burton et al. 2003; Allard

et al. 2005; La Spina et al. 2010, 2015). Furthermore, by treating each spectrum as an individual measurement (La Spina et al. 2015; Oppenheimer et al. 2018), we examined the variations in gas composition during the explosive activity.

### Field surveys

Two surveys aimed at evaluating the dispersal of the tephra deposit from Catania up to the summit and eastern slopes of Etna and at collecting related samples were conducted. Our first survey began at 08:00 UTC on 24 March covering a SW-S dispersal area, where the fallout was over for a few hours, going from the distal deposits (typically more ephemeral and removable) towards the most approachable proximal deposits. The lava fountaining had, in the meantime, shifted towards a pulsating Strombolian activity accompanied by a continuous ash emission, and the eruption column was now clearly bent over the SE flank of Etna. After 12:00 UTM, when the fallout was completely ended, we also surveyed the remaining area between S and SE affected by tephra deposit. The day after, we completed our fieldwork on the summit slope from Rifugio Sapienza (1920 m a.s.l.) up to Belvedere (~2660 m a.s.l.). In all, we collected 34 samples (from SEC-240321-0 to SEC-240321-33) from as many different sites on measured surfaces ranging from 0.04 to 1.16 m<sup>2</sup> (Table 1).

### Laboratory analyses

Samples were first dried in the oven at 55 °C for 12–24 h at the INGV-OE Sedimentology and Optic Microscopy Laboratory, and then weighed to estimate the mass loading per square meter before being subjected to further analyses. Grain size measurements were carried out on 32 samples at 1/2  $\phi$  intervals ( $\phi = -\log_2 d$ , where  $d$  is the particle diameter in mm) by CAMSIZER (Retsch), a particle size and shape analyser (Lo Castro and Andronico 2008). The instrument also provided coeval quantitative information of the ‘sphericity’ shape parameter (defined as  $SPHE = 4\pi A/U^2$ , where  $A$  is the area and  $U$  is the perimeter of a particle projection) for each measured granulometric class, of which we used the average value of each class of particles as input data for numerical simulations (see next section). This formula is defined as sphericity also by several other authors (e.g. Riley et al. 2003; Leibrandt and Le Pennec 2015; Miwa et al. 2015).

At the laboratory of INGV, Sezione di Pisa (INGV-PI), samples SEC-240321-0 (Piazza Bovio), SEC-240321-6 (Camporotondo) and SEC-240321-20 (Fleri 2) were sieved by a mechanical agitator at 1  $\phi$  size interval and observed by means of stereomicroscope for component analysis. Fragments > 0.125 mm (3  $\phi$ ) were divided into juvenile,

lithic and loose crystal components by describing both their whole aspect (colour, iridescence, occurrence of adhering secondary minerals) and external shape. From each studied sample, a selection of about 50 clasts identified as ‘juvenile’, i.e. fresh material, was hand-picked from the size interval 0.5–1 mm (1  $\phi$ , coarse ash; White and Houghton 2006) and neatly arranged on a double-adhesive, carbon-coated tape mounted on a glass slide, following the method described in Cioni et al. (2008). For morphological analysis, an image of each clast was acquired at INGV-PI with a Zeiss Evo MA 10 scanning electron microscope (SEM), working in secondary electron (SE) mode. Morphological parameters of the external perimeter of fragments were obtained on binary images, extracted from SEM-SE images using the ‘Subject’ analytical tools of the Adobe Photoshop® software and processed using the ImageJ software (Schneider et al. 2012). The plane projection of the particle outline was considered for the calculation of four shape parameters, useful to effectively account for the different aspects of the clast morphology: elongation (ELNG; the ratio between the (maximum Feret diameter)<sup>2</sup> and the area of the particle projection), solidity (SLD; the ratio between the area of the particle projection to the area of its convex envelope), convexity (CVX; the ratio between the perimeter of the convex envelope to the perimeter of the particle projection) and SPHE (as for the CAMSIZER, the ratio of the circumference of a circle equal to the particle’s projected area to the square of the perimeter of the particle). Textural and compositional analyses were performed on the same glass slides, after gluing them with epoxy resin and polishing in order to expose the inner portion of fragments, as wide a surface as possible. High-resolution (3072 × 2304), back-scattered electron (BSE)-SEM images, at a magnification of × 300–500, were acquired for groundmass texture investigation. Vesicle- and microlite-forming groundmasses were isolated by processing BSE-SEM images using a combination of tools available in Adobe Photoshop®. The area fraction, size and shape of vesicles and the microlite content (area fraction %) were derived by means of the ImageJ software. Glass and mineral compositions were determined on the same clasts by means of the Zeiss Evo MA 10 SEM, equipped with an Oxford ISIS microanalytical energy-dispersive spectroscopy (EDS) system. About 15 ash fragments were analysed per sample, and the results are reported as an averaged composition of 2 or 3 analyses per fragment. The accuracy of EDS analyses was checked by routinely analysing the reference basaltic glass VG2 (Gill et al. 2016), and the results were < 3–4% for most of the major elements and < 5% for Na<sub>2</sub>O. To ensure that our dataset is comparable with those obtained in other laboratories and with different analytical systems, the element concentrations were normalised to the VG2 reference value, using the formula  $C_{\text{norm}} = C_{\text{measured}} \times ki$ , where  $ki$  is the ratio between the standard reference value/average of  $n$ . Ten measurements

**Table 1** List of samples with associated locations, UTC coordinates, elevation above sea level, distance from the vent and mass load per square meter

Sample	Location	Latitude (decimal degrees)	Longitude (decimal degrees)	Elevation (m a.s.l.)	Distance from the vent (km)	Mass load (g/m <sup>2</sup> )
SEC-240321-0	Piazza Bovio	37.509583	15.093864	27	27.8	49.6
SEC-240321-1	INGV-OE	37.513499	15.082160	46	27.0	62.2
SEC-240321-2	Misterbianco	37.520496	15.015624	161	26.2	218.7
SEC-240321-3	Motta S. Anastasia	37.522527	14.969195	290	25.4	72.3
SEC-240321-4	Etnapolis	37.546529	14.947984	251	23.0	73.6
SEC-240321-5	Paternò	37.555731	14.904114	241	21.9	1.0
SEC-240321-6	Camporotondo	37.568793	15.007890	434	20.0	307.8
SEC-240321-7	S. Pietro Clarenza	37.573880	15.019373	475	19.5	397.8
SEC-240321-8	Belpasso	37.578863	14.982300	487	18.9	149.2
SEC-240321-9	Borrello	37.602149	14.984955	638	16.2	243.2
SEC-240321-10	SP120—Feudo	37.627733	14.986133	866	13.5	644.5
SEC-240321-11	Chiesa S. Leo	37.641602	14.988145	998	12.0	330.9
SEC-240321-12	La Quercia	37.669123	14.987224	1292	8.9	235.7
SEC-240321-13	Piano Vetore	37.690794	14.978810	1715	6.7	853.0
SEC-240321-14	Rifugio Sapienza	37.699854	14.999569	1906	5.4	5476.2
SEC-240321-15	Schiena dell'Asino	37.700116	15.012658	1802	5.5	4303.6
SEC-240321-16	Post-Schiena dell'Asino	37.698733	15.018652	1768	5.7	3259.2
SEC-240321-17	<i>Post-Case del Vescovo</i>	37.696542	15.044021	1466	7.0	188.6
SEC-240321-18	Lady Ceramica	37.666324	15.099014	553	12.7	24.4
SEC-240321-19	Fleri 1	37.659509	15.097809	525	13.2	104.4
SEC-240321-20	<i>Fleri 2</i>	37.663929	15.097170	541	12.8	65.8
SEC-240321-21	Monterosso	37.643782	15.092862	518	14.1	193.4
SEC-240321-22	Cono 2001	37.724059	15.006155	2603	2.6	9815.8
SEC-240321-23	Belvedere	37.728422	15.008606	2665	2.2	8713.2
SEC-240321-24	Montagnola	37.717688	15.006598	2614	3.3	6240.1
SEC-240321-25	Montagnola 2	37.717131	14.995630	2418	3.4	5058.7
SEC-240321-26	Calcarazzi	37.708398	14.996254	2160	4.4	8122.2
SEC-240321-27	Mascalucia	37.564095	15.032810	395	20.6	302.0
SEC-240321-28	Nicolosi INGV-OE	37.613535	15.019414	724	15.1	754.7
SEC-240321-29	Pedara	37.609869	15.055244	587	16.1	183.6
SEC-240321-30	Trecastagni	37.619933	15.073122	600	15.7	195.5
SEC-240321-31	Fleri 3	37.659445	15.097886	526	13.2	63.2
SEC-240321-32	Poggio Felice	37.666323	15.098971	552	12.7	8.5
SEC-240321-33	Tremestieri	37.569716	15.071130	360	20.8	196.9

All samples were analysed with the CAMSIZER for grain size analyses except the two ones reported in italic, i.e. SEC-240321-17 (Post-Case del Vescovo) and SEC-240321-20 (Fleri 2)

were performed at SEM during the analytical sessions (Pompilio et al. 2017). The whole compositional dataset is presented as Supplementary Tables S2, S3, S4 and S5.

### Eruption source parameters by the tephra fallout deposit study

The total grain size distribution was calculated using the Voronoi tessellation method (Bonadonna and Houghton 2005) from 32 samples collected on the ground. The procedure also requires the isoline of zero mass, which has

been set based on satellite images of the tephra plume. The Voronoi cells computed for the sampling points are shown in Supplementary Fig. S1, and their areas, multiplied by the mass loadings, have been used as weights to compute the total grain size distribution.

The total erupted mass was estimated by four different methods, i.e. the straight-line exponential fit (Pyle 1989), the two-segment fit (Fierstein and Nathenson 1992), the power-law fit (Bonadonna and Houghton 2005) and the Weibull distribution (Bonadonna and Costa 2012) (Fig. S2). All these methods are based on fittings of thickness vs (area)<sup>1/2</sup> values,

which are computed from isomass/isopach contours of the fallout deposit. Here, the contours have been computed from an interpolation of the 32 thickness values sampled from the deposit and the points defining the isoline of zero mass (the same points used for the Voronoi tessellation). To this end, the Python library PyKriging has been applied to perform a universal kriging spatial interpolation (Zimmerman et al. 1999). For this application, a linear variogram produced the best results to estimate the autocorrelation between the samples. While ordinary kriging assumes that the variation of the variable does not depend on the direction, for a tephra deposit, it is common that there is a direction with a major influence on the distribution of thickness values, associated with the prevailing wind. This has been taken into account in the fitting by adopting an anisotropic kriging (Hansen 1993). The interpolation surface obtained with this approach has been used to compute the isomass contours, and thus the total erupted mass with the different fitting methods listed above.

## Numerical modelling

The numerical models PLUME-MoM-TSM (de' Michieli Vitturi and Pardini 2021) and HYSPLIT (Stein et al. 2015) were used to simulate the release, atmospheric transport and deposition of the tephra particles erupted during the 23–24 March 2021 episode.

PLUME-MoM-TSM is a steady-state integral eruption column model that simulates the dynamics of volcanic columns in a 3D coordinate system. The eruption mixture formed by solid tephra particles and gases (mainly water vapour) is released from the vent source with certain initial conditions (which include plume radius, initial velocity and temperature) and rises through the atmosphere until a maximum height is reached. PLUME-MoM-TSM is a wind-affected model. This means that the model accounts for the atmospheric profile above the vent, whose characteristics in terms of wind velocity, atmospheric temperature and humidity affect the model results. Tephra particles can be either lost by the column during the ascent or reach the neutral buoyancy height. At this height level, PLUME-MoM-TSM simulates the initial spreading of the umbrella cloud as a gravitational current (Webster et al. 2020), in order to estimate the upwind spreading of the plume. To simulate the subsequent atmospheric transport and ground deposition of the particles, we coupled PLUME-MoM-TSM with the tephra transport and dispersal model HYSPLIT. In particular, the solid particles leaving the column from the vent to the neutral buoyancy level are injected into the atmosphere from point sources located on the column axis. The solid particles reaching the neutral buoyancy height enter the atmosphere from a circular area source which best fits the position and upwind spreading of the umbrella cloud.

The coupling between the two codes is done automatically through a workflow written in Python that creates the input file of HYSPLIT from the results of PLUME-MoM-TSM. A detailed description of this procedure and application examples can be found in Pardini et al. (2020, 2023), Tadini et al. (2022) and references therein.

In this work, the above-mentioned numerical workflow was used in conjunction with an optimization procedure to retrieve the height time series of the eruption column able to produce the best fit with the 23–24 March 2021 episode. The optimization function to minimize is based on the difference between simulated and observed values of the tephra ground load at the 34 sampling locations, and the optimization algorithm used for this application is based on an evolutionary algorithm through the toolkit DAKOTA (Adams et al. 2014). A similar analysis is presented and discussed in detail in Andronico et al. (2021b).

## The 23–24 March 2021 eruptive activity

The 23–24 March 2021 paroxysm was the 16th of a sequence of 17 episodes taking place from 16 February to 1 April. Figure 2a and b shows the pattern of the RMS amplitude of volcanic tremor from 1 February to 1 April 2021 and a detail of the studied episode, respectively, while in Fig. 2c, the tremor patterns of all the single episodes overlapping each other are shown.

The chronology of the 23–24 March paroxysm is based on the analysis from the video recordings acquired by six INGV-OE surveillance cameras (visible and thermal; Fig. 1) and their correlation with the volcanic tremor pattern (Fig. 2b), and direct observations carried out in the field. Cameras are located around Etna from ~140 m a.s.l. (in Catania) up to ~2600 m a.s.l. (at La Montagnola) (Fig. 1). Most of the eruptive activity took place during the night with little or no visibility from the visible cameras, but also the frequent atmospheric clouds partially or totally obscured both the visible and thermal cameras, thus preventing us from describing the temporal evolution of the eruptive activity in greater detail. Figure 3 shows the evolution of the eruptive activity between 22:23 UTC (=local time – 1) on 23 March and 08:45 UTC on 24 March.

Following about 4 days of interval time from the previous paroxysmal episode on 19 March, the volcanic tremor had started to increase with an irreversible trend after 18:50 UTC (Fig. 2a, b). The resumption of explosive activity at the SEC was observed at least from 19:01:30 by the EMV camera (Fig. 2b). The opening vent was located in the eastern summit portion of the SEC, exactly inside the depression that at the time cut the portion of the cone from the middle-eastern flank to the summit. After 20:25 UTC, incandescent products started to be ejected discontinuously outward on the

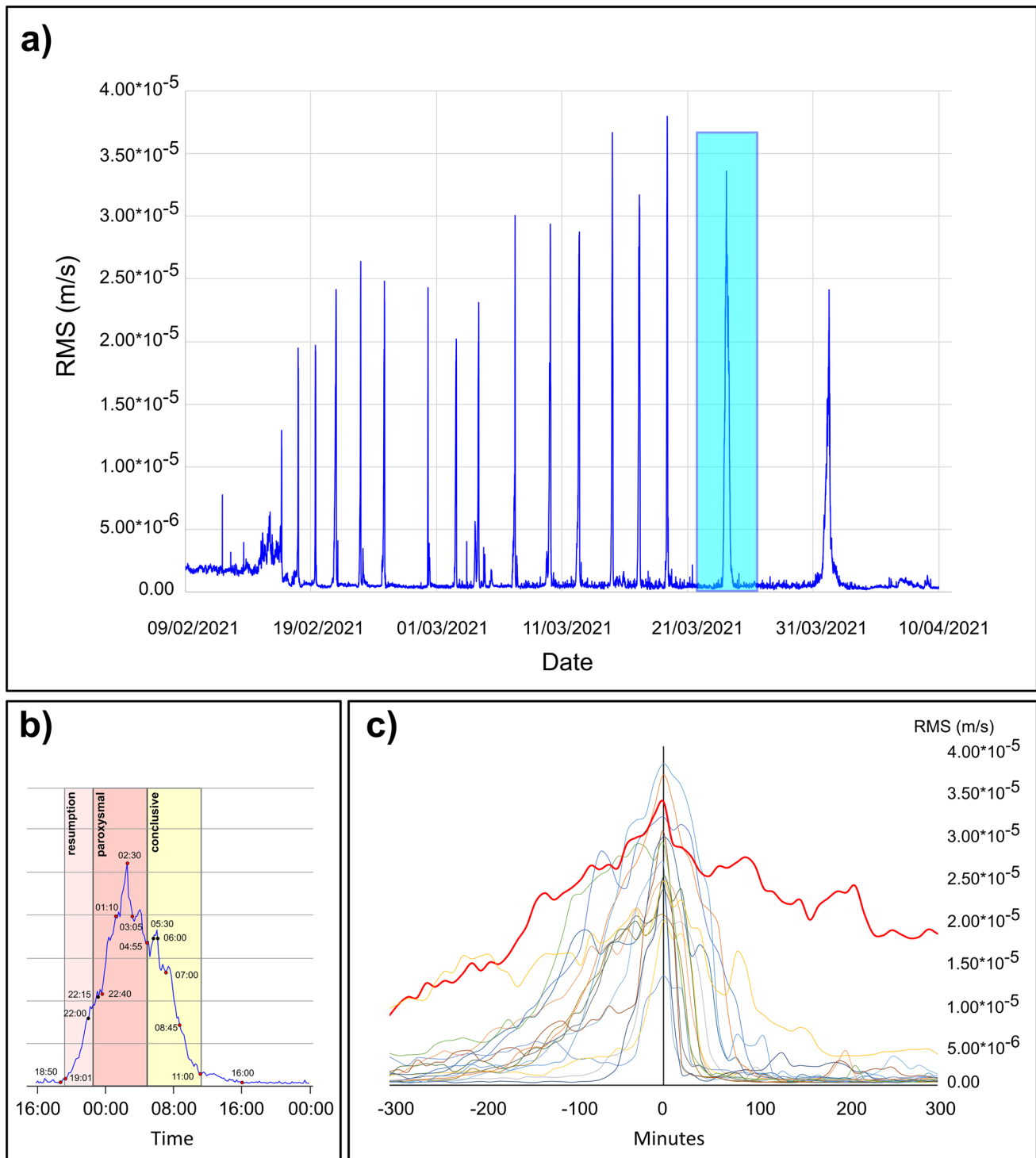


**Fig. 2** Pattern of the volcanic tremor. **a** In the period 1 February–1 April 2021 (the light blue box shows the studied episode). **b** During the 23–24 March 2021 paroxysm (see text for details). **c** The volcanic tremor of the 17 episodes overlapping each other and centred on the

maximum peak value of root mean square (m/s) at time 0, with the thick red line showing the 23–24 March episode. On the sides of the y-axis, the time expressed in minutes before and after the maximum peak value of the tremor is reported

summit rim of the cone by episodic bursts much higher and wider than before. After 21:15 UTC, the outer southern rim and the upper part of the depression displayed an incipient

carpet of incandescent coarse bombs, whose area gradually extended with time down the slopes of the cone. A gas-dominated plume was approximately dispersed to the west,

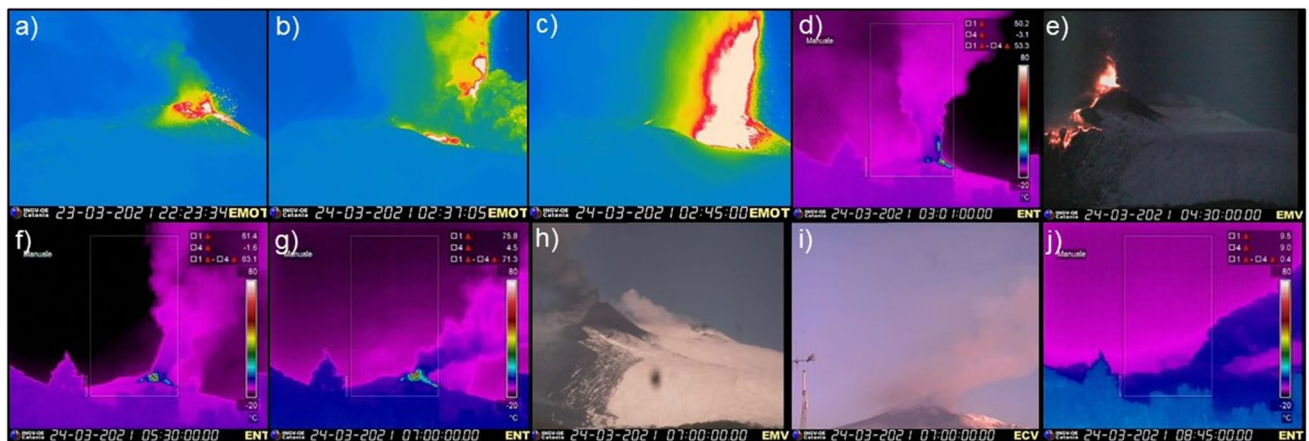


**Fig. 3** a–j Chronology of the 23–24 March 2021 paroxysm by surveillance cameras (see text for detail description)

while occasionally, the gas plume from the summit crater Bocca Nuova also appeared incandescent. After 22:00 UTC, the explosions became frequent enough (i.e. 1 every 5–10 s) to make the explosive activity continuous, and ejected abundant incandescent material up to a maximum height of about 150 m above the cone (Fig. 3a). Between 23:00 and 23:15 UTC, violent Strombolian jets began to alternate with almost sustained lava fountains, which became predominant after 23:40 UTC (Fig. 2b), exceeding 200 m in height. This escalation of eruptive activity paralleled an incessant rising of the volcanic tremor (Fig. 2b). Incandescent, narrow tongues composed of coarse bombs began to flow from the S rim down the upper slopes, too.

The video-camera recordings indicate the most intense explosive phase between 01:10 and 03:05 UTC of 24 March (Fig. 2b), with maximum frequency (up to 1 explosion per s), width and height of magma jets (rising 250 m and further above the SEC) confined from 02:25 to 02:50 UTC (Fig. 3b–d). After 03:05 UTC, the paroxysmal activity started a gradual waning trend in terms of intensity (i.e. height of jets and abundance of ejected products), with only a short attempt at an intense resumption of the lava fountains between 03:28 and 03:32 UTC. Indeed, although the magma jets decreased in intensity, the fountaining activity remained sustained at least up to 04:30 UTC (Fig. 3e) and only after 04:55 UTC was it replaced by discrete Strombolian explosions up to 100–150 m, with at least 2 active vents clearly visible above the SEC. The jet heights further decreased up to < 100 m after 05:30 UTC (Fig. 3f) and at ~ 50 m after 06:00 UTC (Fig. 2b). The explosions continued to drop in intensity and frequency (from one every few seconds to > 10 s) until gradually the ejection of coarse products into the outer crater rims was no longer observed. This activity was accompanied and then dominated by a continuous ash emission from the SEC. After 07:00 UTC, the ash jets enveloped smaller magma-rich bursts; visible and

thermal cameras enabled observing they initially reached approximately 50 m above the crater, then decreasing more and more in size until they were hidden by the ash emission (Figs. 2b and 3 g–i). After 11:00 UTC, the SEC emitted only a sustained gas plume pushed by the wind approximately towards the SE, without any evidence of eruptive activity by INGV-OE surveillance cameras.

The counterclockwise rotation of the eruption plume made the observation of the activity and of the E portion of the cone from the south cameras partially hidden at least from 03:40 UTC until 04:50 UTC, when the plume had now moved SE (for comparison, see Fig. 3d, f, g and Fig. S3). Moreover, the shift of the explosive style from fountaining to Strombolian after 04:55 UTC also corresponded to the now completed transition from a sustained to weak plume after 05:30 UTC (Fig. 3f). Finally, after 08:45 UTC (Fig. 2b), the plume turned to an almost pulsating, narrow and bent ash plume extending SE, which video-camera recordings (Fig. 3j), direct observation (Fig. 5a) and satellite image (Fig. S4) indicate with a height of around 3 km above the summit and width less than 1 km before expanding in width after ~ 6 km from the vent.

By correlating the observation of the eruptive activity with the tremor pattern, we identify the paroxysmal phase from 23:40 UTC on 23 March to 04:55 UTC on 24 March, followed by an unusually long conclusive phase lasting until 11:00 UTC (Fig. 2b). The maximum amplitude of the volcanic tremor was reached at 02:30 UTC, thereafter followed by a continuous decreasing trend, almost symmetrical to the increasing pattern. At 03:20 UTC, the tremor continued its general decline, although alternating with some short periods of ascending trends or with nearly constant amplitude values ranging from 10 to 40 min (Fig. 2b). After 07:20 UTC, the descent was constant; around 16:00 UTC, tremor values comparable to those before the start of the activity were reached, i.e. below  $1 \times 10^{-6}$  m/s (Fig. 2b).



To complete the account of the 23–24 March 2021 lava fountain episode, a lava flow began to descend in the eastern depression at least from 02:21 UTC, very quickly reaching the exit in the lower portion of the cone and propagating in correspondence with the break-in slope, and advanced further towards the upper Valle del Bove (Figs. 1 and 3e) forming some branches fed at least until 06:00 UTC. A secondary lava flow descended down the SW upper depression of the SEC, reached the base of the cone and then flowed to the E for a few hundreds of meters (INGV-OE 2021). Finally, at 02:36 UTC, the INGV-OE thermal recordings showed a hot ground-hugging ash cloud spreading from E to W on the eastern summit slope, which temporarily obscured the SEC (Fig. 3b). Based on their high recurrence observed over the last years at Etna, these phenomena are commonly related to the sudden flow of volcanic materials due to different triggering mechanisms (e.g. Andronico et al. 2018; INGV-OE 2022a). In this specific case, we believe that a hot avalanche was formed due to the presence of the active lava

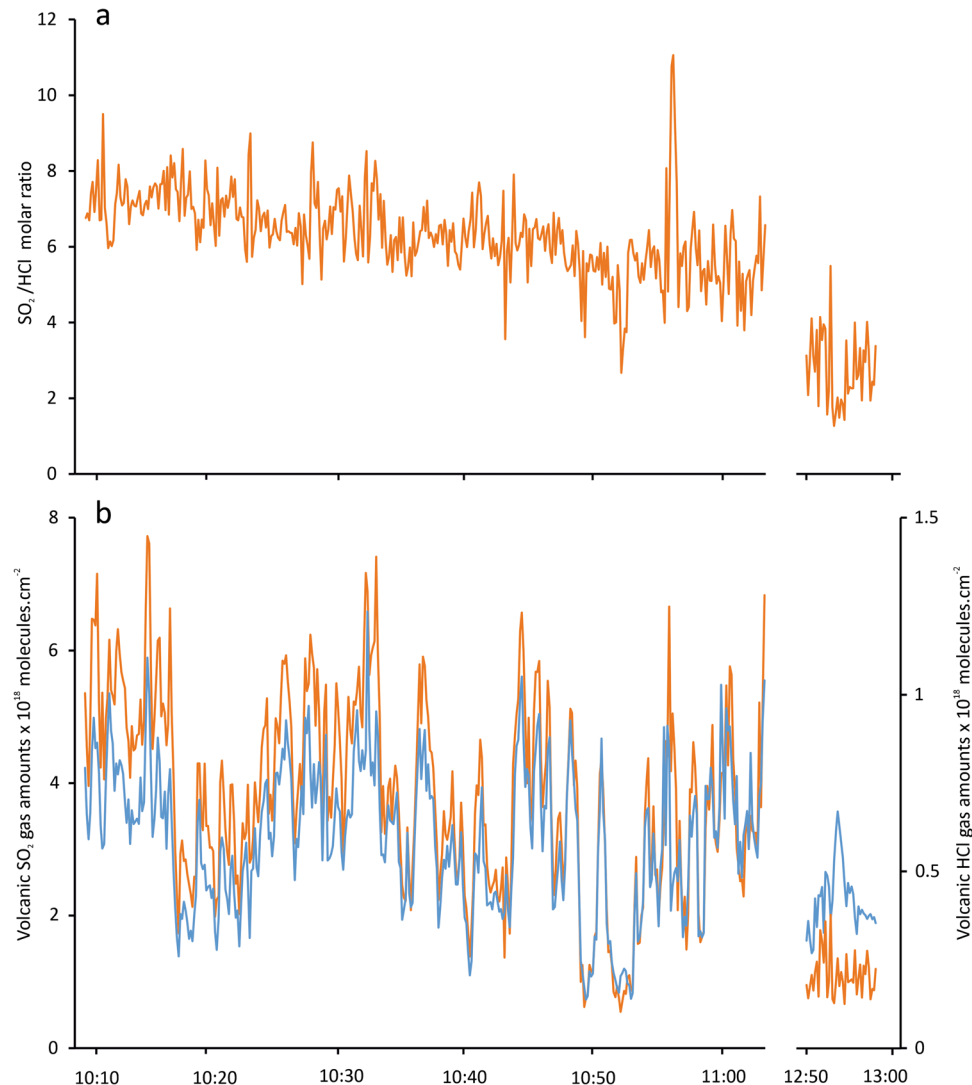
flow on the steep slope of the cone, which possibly caused a relatively small collapse of the upper portion of the SEC as well as having involved pyroclastic material coming from the lava fountain.

## Results

### Gas geochemistry of eruption plume

The retrieval of solar occultation OP-FTIR measurements, performed on the morning of 24 March, allowed us to draw the temporal evolution (every 8 s) of gas phase, in terms of  $\text{SO}_2$  and HCl, in the conclusive phase of the eruption, i.e. when both seismic tremor and eruptive activity dropped gradually. The upper part of Fig. 4 illustrates the evolution of  $\text{SO}_2/\text{HCl}$  molar ratio. The  $\text{SO}_2/\text{HCl}$  ratio shows a decreasing trend from 8 to 2 between 10:10 and 13:00 UTM on 24 March. The decreasing trend of the ratio is attributable to

**Fig. 4** Variation, during the last part of paroxysmal activity, of **a**  $\text{SO}_2/\text{HCl}$  molar ratio and **b**  $\text{SO}_2$  (orange) and HCl (blue) magmatic gas amounts



the relative decrease in the quantities of  $\text{SO}_2$  compared to HCl, as shown in the lower part of the figure in which the evolution of the retrieved magmatic gas is plotted. A trend with a greater quantity of gas coinciding with the occurrence on the surface of explosions typical of Strombolian activity is evident.

## Tephra deposit features

### Tephra fallout dispersal and grain size distribution

During the paroxysmal episode, the wind direction shifted from SSW to SE, the change occurring after 05:00 UTC in the morning of 24 March (Fig. 5a and Fig. S4). This had significant implications on the dispersal of the eruption plume in the atmosphere, consequently increasing the area affected by the tephra fallout as well as the ground load.

In detail, at 07:00 UTC of 24 March the fallout was already over in the area from S to SSW with respect to the SEC (Figs. 1 and 5a). Inside the city of Catania, i.e. slightly eastward the dispersal axis of the paroxysmal phase, we collected from 49 to 62  $\text{g}/\text{m}^2$  of tephra at distances of  $\sim 27$ – $28$  km from the vent (samples SEC-240321-0 and SEC-240321-1; Table 1). The deposit was almost entirely composed of ash particles  $< 1$  mm ( $0 \varphi$ ), with mode at 0.25–0.5 mm ( $2 \varphi$ ) ranging from 64 to 67%. Approaching the SEC along the dispersal axis, we found about 200  $\text{g}/\text{m}^2$  at Camporotondo-S. Pietro Clarenza (20–19.5 km; SEC-240321-6 and SEC-240321-7); samples were coarser-grained, although most of the particles were smaller than 2 mm, with 57.9–60.5% between 0.5 and 1 mm ( $1 \varphi$ ). At  $\sim 15$  km from the vent (Nicolosi; SEC-240321-28), the deposit was made of 755  $\text{g}/\text{m}^2$  of coarse ash (70%  $> 0.71$  mm,  $0.5 \varphi$ ; 42%  $> 1$  mm,  $-1 \varphi$ ) (Fig. 5a).

Advancing towards the summit area, we measured a tephra deposit of 5.5  $\text{kg}/\text{m}^2$  at Rifugio Sapienza (5.4 km; SEC-240321-14), consisting of more than 65% of lapilli between 2 and 8 mm (from  $-1$  to  $-3 \varphi$ ), and of 9.8  $\text{kg}/\text{m}^2$  close to Cono 2001 (2.6 km; SEC-240321-22), where 70% of clasts was larger than 4 mm ( $-2 \varphi$ ; Fig. 5b).

At Fleri (13.2 km SE from the SEC, i.e. laterally with respect to the dispersal axis; sample SEC-240321-31), the fallout related to the conclusive phase of the event started to cover houses and roads only after 06:00 UTC. Here, the deposit is composed of medium ash (more than 70% of particles in the range 0.25–0.5 mm ( $2 \varphi$ ); White and Houghton 2006) and a relatively low mass load per square meter (63 g) if compared to the tephra fallout found in Nicolosi. To note, the same values of mode ( $2 \varphi$ ) and similar sorting (moderately well sorted according to Gradistat software; Blott and Pye 2001) resulted for samples SEC-240321-0 and SEC-240321-1 (collected in Catania at  $\sim 27$ – $28$  km from the vent) and sample SEC-240321-31 (collected in Fleri at  $\sim 13$  km).

### Eruption source parameters

We retrieved the total grain size distribution and the particle sphericity from the CAMSIZER analyses of the tephra samples, and used these data as inputs for the numerical simulations. The total grain size distribution reconstructed by applying the Voronoi tessellation method shows bimodality with peaks at  $-1.5$  and  $1.5 \varphi$  (Fig. 6a). By fitting the total grain size distribution with two Gaussian functions, we obtained a bimodal distribution with the major mean at  $-1.471 \varphi$  (standard deviation =  $1.298 \varphi$ ) and the minor one at  $1.365 \varphi$  (standard deviation =  $0.638 \varphi$ ), with a fitting coefficient of determination ( $R^2$ ) of 0.9964 and a root-mean-square error (RMSE) of  $6.1e^{-3}$ . Note that the fitting has a

**Fig. 5** **a** The eruption plume bent to the SE of Etna as appeared at about 09:00 UTC from Motta S. Anastasia, 25.4 km SSW from the SEC. **b** The fine-grained, not-continuous coarse ash deposit at Chiesa S. Leo (sample SEC-240321-11), 12 km SSW from the SEC and  $\sim 3$  km above the Nicolosi sampling site. **c** The 3-cm-thick tephra fallout deposit collected at Belvedere (sample SEC-240321-23), at 2.2 km SSE from the SEC on the snow cover and 600 m above the Cono 2001 sampling site



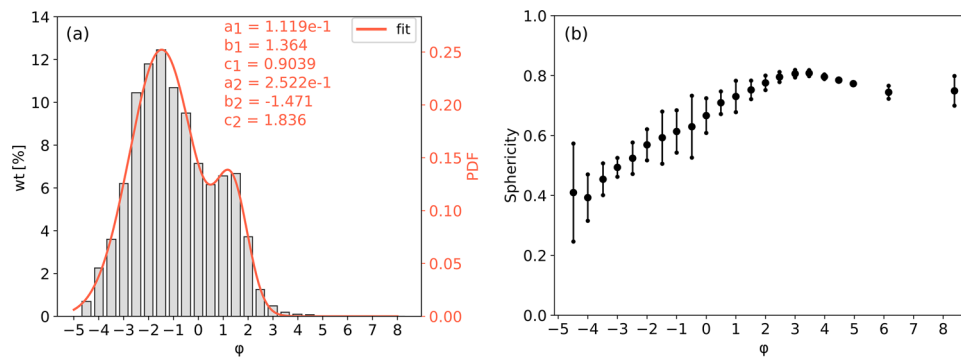


**Fig. 6** **a** Total grain size distribution of the 24 March 2021 episode reconstructed by applying the Voronoi tessellation method (Bonadonna and Houghton 2005). The red line indicates the probability density function (PDF) of the bimodal distribution obtained from the fitting of the discrete distribution (wt% on the left y-axis). Coefficients  $a_1$  and  $a_2$  are related to the height of the peaks of the two

Gaussian functions forming the PDF,  $b_1$  and  $b_2$  to their location and  $c_1$  and  $c_2$  to their width. **b** Particle sphericity derived from the CAM-SIZER analysis. For each particle class, black dots indicate the mean value, while error bars show the uncertainty on the retrieved sphericity value

different y-scale with respect to the total grain size distribution histogram, since the fitting function represents a probability density (i.e. with integral equal to 1).

The sphericity of each class of tephra particles was computed as a mean value (black dots of Fig. 6b) and a standard deviation (error bars of Fig. 6b). From this analysis, it appears that coarser particles have lower sphericity (0.4 on average for the  $-4.5 \varphi$  class) and larger variability than finer ones (0.8 on average for the  $3 \varphi$  class). Indeed, sphericity values range from 0.4 for  $-4.5 \varphi$  to 0.8 for  $3 \varphi$ . Because the standard deviations of the sphericities are relatively small, we used the mean values for all the classes of particles modelled by the numerical simulations.

We estimated the total erupted mass by adopting the four previously described methods (i.e. straight-line exponential fit, two-segment fit, power-law fit and Weibull distribution) and assuming that the density of the erupted products is  $1000 \text{ kg/m}^3$  (following Aubry et al. 2021). The mean value that we obtained is  $8.03 \pm 2.38 \times 10^8 \text{ kg}$  (Table S6). By comparing the obtained results with each other, all the different estimation methods for the total erupted mass produce comparable results, within a range between  $4.79 \times 10^8$  and  $1.15 \times 10^9 \text{ kg}$ . However, by looking at the goodness of fit (see also the fit plots in Fig. S2), we can see that the two-segment fit and the power-law fit better reproduce the observed thickness decay.

By camera recordings and direct observations made from the ground and from space, we derived the duration of the eruptive episode (i.e. when the eruption column is sustained and tephra particles are released from it). Therefore, a total duration of 12 h (from 23:00 UTC on 23 March 2021 to 11:00 UTC on 24 March 2021) was considered responsible for the distal tephra fallout by the volcanic cloud from the slopes of Etna and beyond. This period is actually very long and represents well the temporal evolution of the eruption

column. Finally, by dividing the ground-based total erupted mass per 12 h, we obtain an average mass eruption rate of  $1.85 \pm 0.55 \times 10^4 \text{ kg/s}$ .

## Textural features of erupted products

### Ash componentry and morphology

Ash and lapilli related to the paroxysmal phase are almost entirely juvenile fragments, with less than 3 vol% of clasts below 0.5 mm represented by red and grey lithics. Rare loose phenocrysts of olivine, and subordinate plagioclase, are present in the size fractions below 1 mm. In the size fraction above 1 mm, the two studied samples (SEC-240321-6 and SEC-240321-0) are made up of fluidal fragments with elongated bubbles (Fig. 7a, b) and light-coloured glass. Below 1 mm, a lighter and more vesicular juvenile component appears (Fig. 7c–f and Fig. S5a, c). In the SEC-240321-0 sample, at  $\sim 28 \text{ km}$  from the vent, all particles larger than 0.5 mm are juvenile with similar features to those of sample SEC-240321-6. In both samples, fluidal clasts often have protruding filaments at the edges (Fig. 7g–i), and small bubbles can be present on the clast surfaces. In sample SEC-240321-20, erupted during the conclusive phase of the eruption, clasts larger than 1 mm are all juveniles and can be grouped in two types: the first type has a light honey glass and varies between elongated fluidal to equidimensional particles (Fig. 7j), with smooth to vesicular surfaces, and the second type has a dark glass and varies between smooth external surfaces to irregularly shaped particles. In this sample, fluidal fragments lack the protruding filaments that typify the first phase of the eruption. Many secondary minerals adhere on the clast's external surfaces (Fig. 7k). However, glasses appear almost fresh. Below 1 mm, juvenile clasts

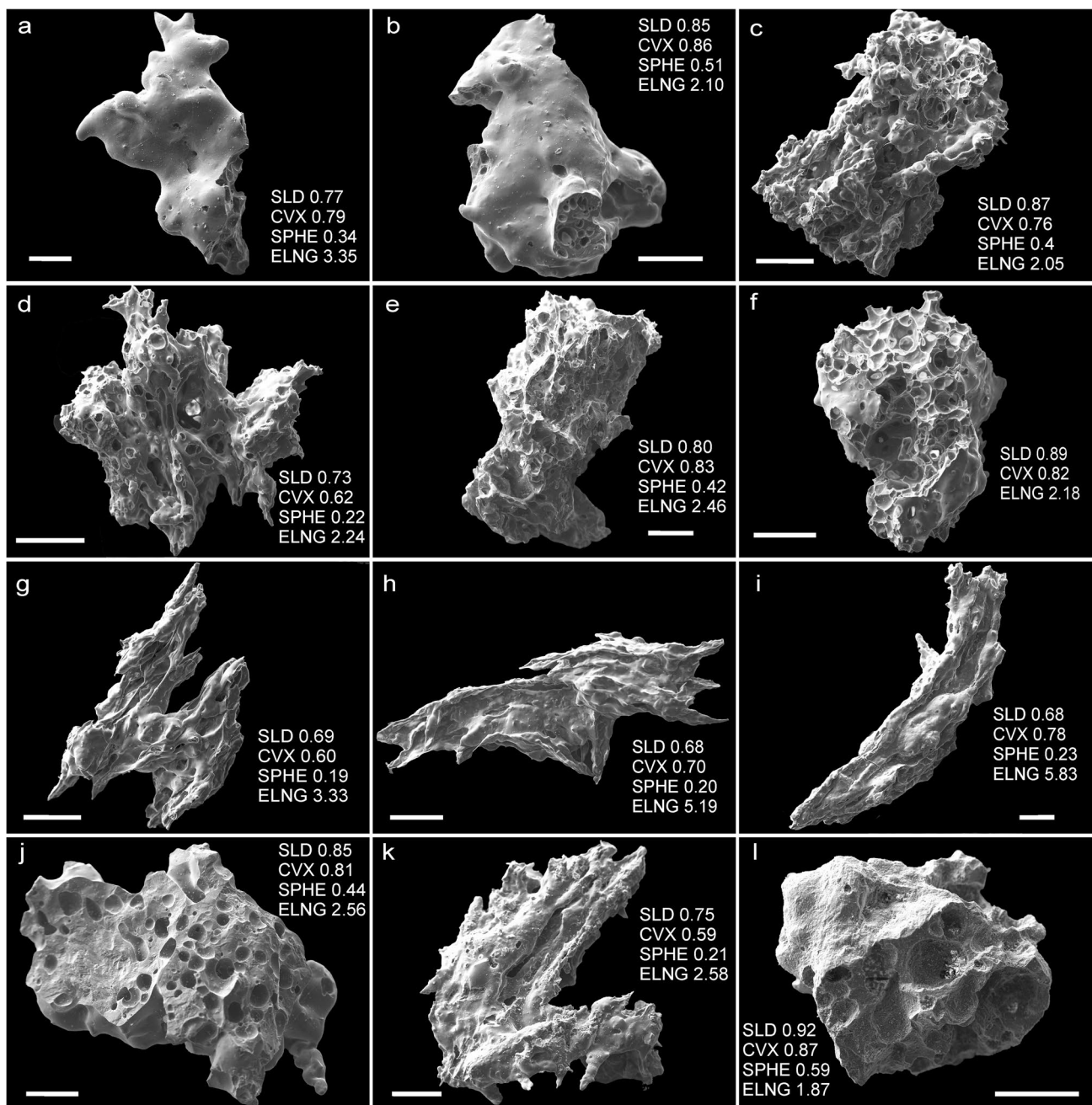


**Fig. 7** SEM images of particles representative of samples SEC-240321-0 (**a, b, g, h**), SEC-240321-6 (**c-f**), and SEC-240321-20 (**j-l**) in the size fraction 0.5–1 mm (1  $\phi$ ), showing the variability of morphological features. **a, b** Fluidal with smooth surfaces; **c, f** vesic-

ular; **g-l** fluidal with spiny surfaces; **j** composite; **k, l** recycled. Shape parameter quantification is reported for each particle. SLD, solidity; CVX, convexity; SPHE, sphericity; ELNG, elongation. See text for details on calculation of measurements. Scale bars = 250  $\mu$ m

represent less than 10 vol% of the particles, and recycled and lithic clasts become predominant (Fig. S5c, d). Juvenile fragments are similar to those present in the coarser material, while recycled clasts (e.g. ash particles which, after being erupted, fall back into the conduit/crater and are recycled by subsequent explosions; Houghton and

Smith 1993) are dark-coloured, with a glittered external aspect and partially eroded external surfaces (Fig. 7l and Fig. S5c, d). However, the inner portions of these clasts seem to be unaltered, suggesting that only a low degree of intra-crater recycling occurred during the conclusive phase of the eruption (D’Oriano et al. 2014).

## Shape parameters of ash particles

Shape parameters, collected on ash fragments between 0.5 and 1 mm ( $1\ \varphi$ ) of size interval, reveal that there are small differences between intermediate (SEC-240321-6) and distal (SEC-240321-0) samples related to the paroxysmal phase of the eruption (Fig. 8a, b). In fact, all particles fall in the field of CVX between 0.6 and 0.93, SLD between 0.65 and 0.92, SPHE between 0.16 and 0.57 and ELNG between 1.69 and 5.89. However, the most distal ash is characterized by lower values of both CVX (mode = 0.82 in SEC-240321-6 and 0.76 in SEC-240321-0) and SLD (mode = 0.9 in both SEC-240321-6 and SEC-240321-0 samples and a second mode at 0.8 in SEC-240321-0), lower SPHE (mode = 0.5 in SEC-240321-6 and 0.4 in SEC-240321-0) and higher ELNG (mode = 2–2.3 in SEC-240321-6, while abundant clasts with ELNG between 2.9 and 5.5 are present in sample SEC-240321-0) (Fig. 8b). Conversely, the shape parameters of ash from sample SEC-240321-20 related to the conclusive phase of the eruption, although varying within the same ranges of the other two samples, show the highest values of CVX (mode = 0.88), SLD (mode = 0.92–0.94) and SPHE (two modes at 0.35 and 0.55), while the ELNG is similar (two modes at 2.2 and 2.6) (Fig. 8a, b). The sphericity of the clasts obtained by measuring the particle projection contour with the ImageJ software (range 0.2–0.7, mode 0.4; Fig. 8) is different from that obtained with the CAMSIZER (range 0.65–0.75, average 0.7; Fig. 6b) in the same class size (0.5–1 mm;  $1\ \varphi$ ). These differences are related to the selection of the type and number of particles, which for the first method are only a few hundreds and representative of the only juvenile material present in each studied sample, while the CAMSIZER analyses all types of particles included in each sample and results were reported as the average of thousands of particles from 32 samples. This means that the CAMSIZER also measures the lithic particles, most of which can have highly circular shapes, as well as the few crystals present in that size fraction.

## Vesicularity, petrography and composition of juvenile fragments

### Quantification of groundmass vesicularity

Juvenile coarse ash (0.5–1 mm) from all the studied samples is characterized by a groundmass with a wide range of vesicularity, spanning from 10–15 to 80 vol%. Vesicles are mainly sub-spherical in shape and often show coalescence of more bubbles separated by thin glassy septa. In some fluidal clasts, large bubbles are deformed and stretched. The sample collected at Camporotondo (SEC-240321-6) is characterized by a vesicularity mostly distributed between 50 and 65 vol%, with a mode peaked at 60 vol% (Fig. 9a). Both

distal and intermediate samples SEC-240321-0 and SEC-240321-20, collected in Piazza Bovio and Fleri, respectively, have a bimodal distribution of vesicularity, with two peaks, at 45 vol% and 60–70 vol%, respectively, where the majority of fragments from the paroxysmal phase (SEC-240321-0) fall in the range > 60 vol%. Most of the clasts from the conclusive phase of the eruption (SEC-240321-20) correspond to the lowest value (Fig. 9a). As a general rule, clast vesicularity and number of bubbles per volume ( $N_v$ ) are positively correlated (Fig. 9b). As a result, the majority of particles from the paroxysmal phase (Camporotondo and Piazza Bovio) are characterized by slightly higher  $N_v$  (average  $1.2 \times 10^3\ \text{mm}^{-3}$ ) with respect to the conclusive phase (Fleri 2;  $8.1 \times 10^2\ \text{mm}^{-2}$ ). In products from both paroxysmal and conclusive phases, vesicle size distribution (VSD) can be described by two linear segments, corresponding to two populations of bubbles (Fig. 9c). The smaller populations (5–200  $\mu\text{m}$ ) have the same slope ( $-3.4 \pm 0.6$ ) and intercept ( $13 \pm 0.3$ ) in all the studied samples, but their maximum size increases from the paroxysmal to the conclusive phase of the eruption, varying from 155 to 161  $\mu\text{m}$  in samples SEC-240321-0 and SEC-240321-6 (Piazza Bovio and Camporotondo, respectively) to 202  $\mu\text{m}$  in sample SEC-240321-20 (Fleri 2; Fig. 9c). The larger populations can be described by a single segment with a slope ranging from  $-21$  to  $-15$  and intercept around 10–11, even if sample SEC-240321-0 shows a third segment attributable to bubble coalescence. Total crystal content and vesicularity are correlated (Fig. 9d), and the lowest vesicularity and highest crystallinity values characterize the particles from sample SEC-240321-20.

### Petrographic features

All fragments are porphyritic, with phenocrysts of plagioclase, pyroxene, olivine and rare oxides in a groundmass mostly made of micron-sized plagioclase, clinopyroxene, olivine and oxides, in order of abundance (Fig. 10a, f). All crystals are euhedral and show direct zoning. Plagioclase is the most abundant phase, varying between 4 and 58 vol% (Fig. 9d). Most phenocrysts of plagioclase have a sieve-textured core and an outer rim with oscillatory zoning, while microlites are elongated and tabular, often broken and partially dislocated. Abundance of mafic crystals (clinopyroxene + olivine + oxides) varies between 0 and 20 vol% (Fig. 9d), except in some fragments from the SEC-240321-20 sample with values from 12 to 32 vol%, which are characterized by large oxides and olivine phenocrysts. Clinopyroxene phenocrysts show sector zoning, while microlites are euhedral and direct zoned. Hopper microlites of olivine, showing elongated morphology, are often present in the groundmass glasses. The rare oxides can be present as phenocrysts or very small microlites. In sample

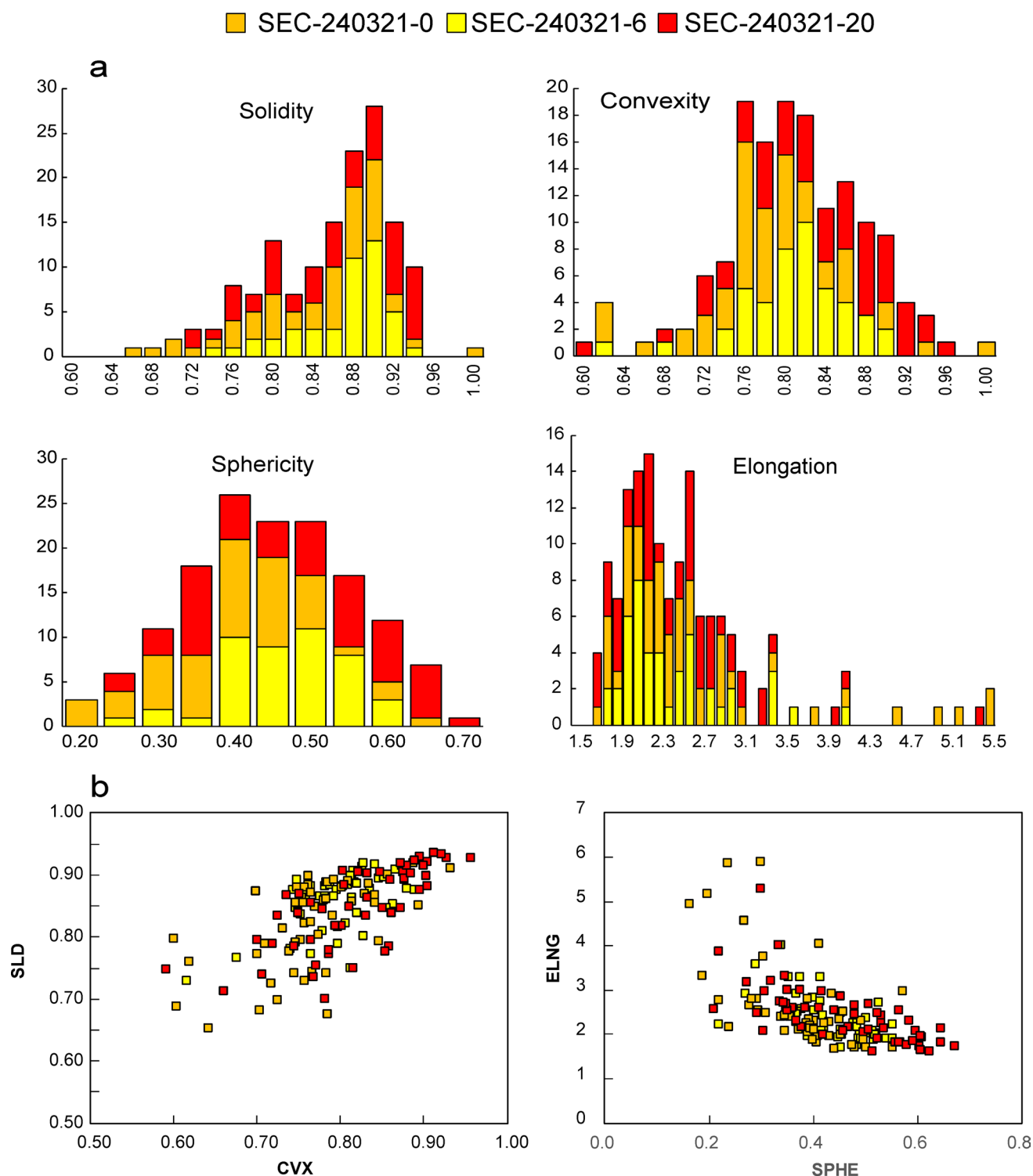


**Fig. 8 a** Histogram of frequency (as the number of particles) of selected shape parameters of coarse ash for three samples: SEC-240321-6 and SEC-240321-0, collected at Camporotondo and Piazza Bovio-Catania, respectively, are representative of the paroxysmal

phase, and SEC-240321-21, collected at Fleri, is representative of the conclusive phase. **b** Solidity vs convexity (SLD-CVX) and sphericity vs elongation (SPHE-ELNG) diagrams

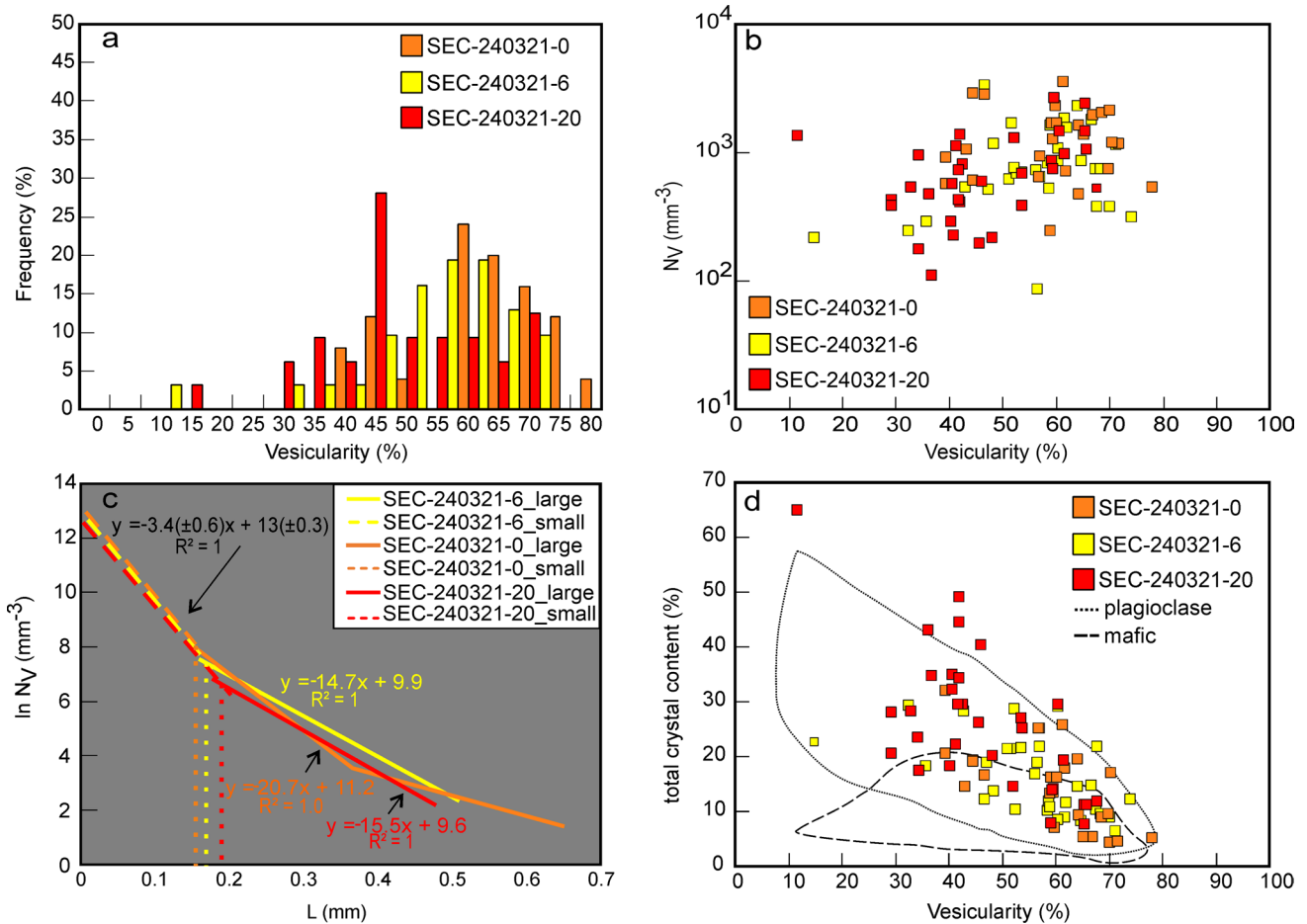


**Fig. 9** Textural quantitative results. **a** Histogram of frequency of clast vesicularity. **b** Vesicularity (%) vs vesicle number density ( $N_v$ ). **c** Classic vesicle size distribution (VSD). **d** Vesicularity (%) vs total

crystal content (plagioclase + olivine + clinopyroxene + oxides). Mafic = olivine + clinopyroxene + oxides

SEC-240321-20, moreover, the coexistence of two glasses with different grey tones in BSE-SEM images and different crystallinity (content and size) was observed in a single clast (Fig. 10f).

**Glasses and mineral composition**

Groundmass glasses of coarse ash from samples SEC-240321-0 and SEC-240321-6 (corresponding to the paroxysmal phase) cover the same range of composition. The narrow variability of major element oxides is characterized by CaO = 8.18–8.49 wt%, MgO = 3.46–3.72 wt%, SiO<sub>2</sub> = 49.41–50.32 wt%, K<sub>2</sub>O = 3.09–3.33 wt%, Na<sub>2</sub>O = 4.25–4.54 wt%, CaO/Al<sub>2</sub>O<sub>3</sub> = 0.49–0.52 and FeO/Mg = 2.88–3.06 (Fig. 11 and Table S2). These results concur with those previously obtained by Corsaro and Miraglia (2022) on the ash sampled from the same event. However, the analyses performed in the present work allow extending the fields of variation, which also include more

evolved compositions (SiO<sub>2</sub> = 49–51.5 wt%). In clast SEC-240321-0, the glass with SiO<sub>2</sub> content of 50.63 wt%, CaO/Al<sub>2</sub>O<sub>3</sub> = 0.48, CaO = 7.72 wt% and MgO = 3.37 wt% corresponds to a microlite-rich portion of the groundmass close to the large phenocrysts of olivine (Fig. 10b). The ash collected during the conclusive phase of the eruption (sample SEC-240321-20) is characterized by a wide range of glass composition, which accounts for both less and more evolved terms with respect to samples related to the paroxysmal phase (Fig. 11a). In particular, within a single clast (sample SEC-240321-20), we found both the more evolved and the less evolved compositions, corresponding respectively to microlite-rich and microlite-poor portions of the groundmass (Fig. 10f).

The analysis of mineral composition indicates that the less evolved olivine has a core of Fo<sub>82</sub> and a rim of Fo<sub>78</sub> (Table S4). Olivine microlites are in the range Fo<sub>74–75</sub> in sample SEC-240321-6. In sample SEC-240321-20, we obtained values of Fo<sub>73–75</sub>, with only a few analyses on the

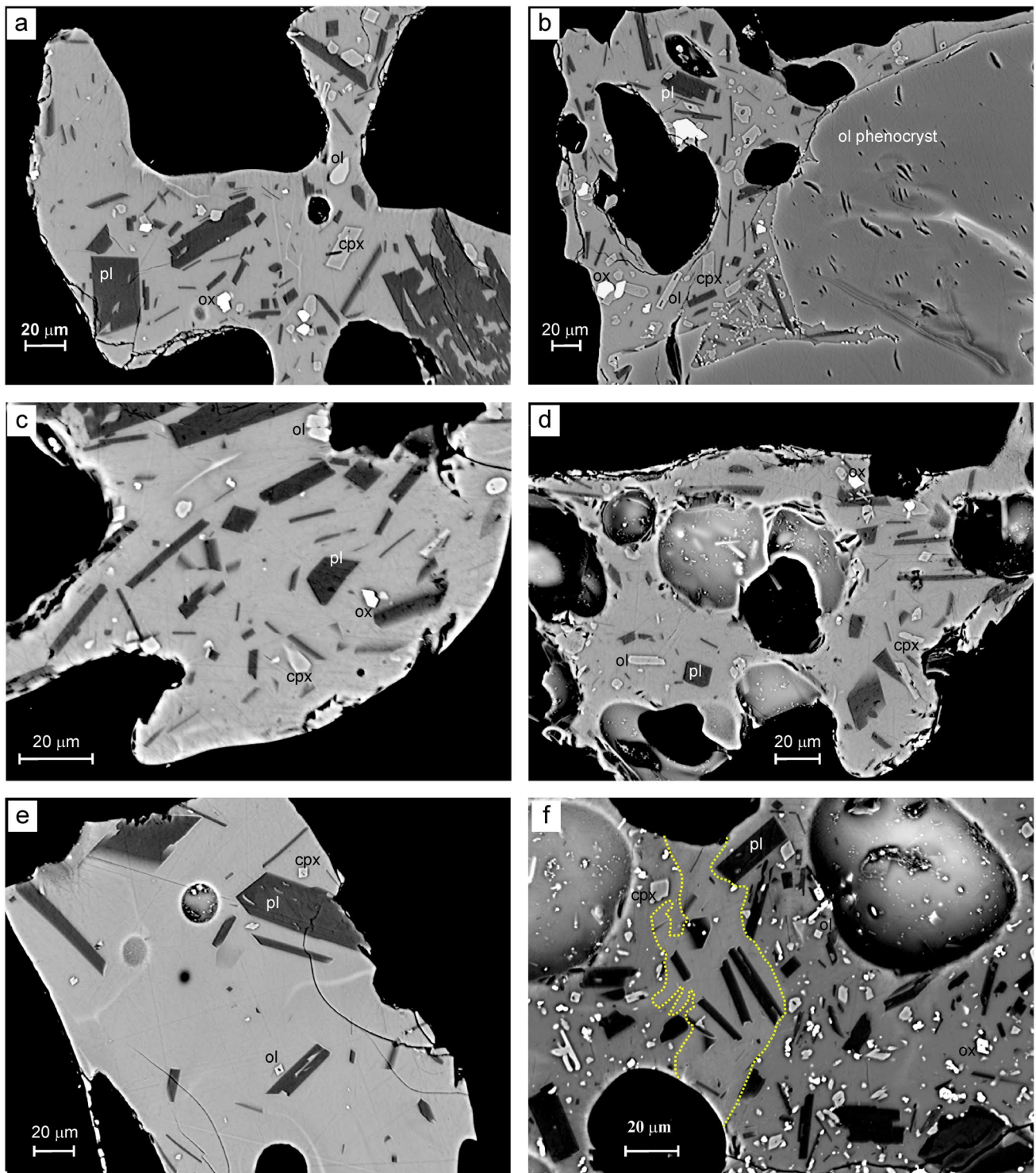


**Fig. 10** BSE-SEM images showing the internal texture of ground-mass glasses in particles representative of the variability of juvenile coarse ash. **a** SEC-240321-6 (Camporotondo). **b, c** SEC-240321-0 (Piazza Bovio). **d–f** SEC-240321-20 (Fleri 2). **e** Mixing texture in

clast from sample SEC-240321-20 corresponding to the conclusive phase of the eruption. pl, plagioclase; ol, olivine; cpx, clinopyroxene; ox, oxides



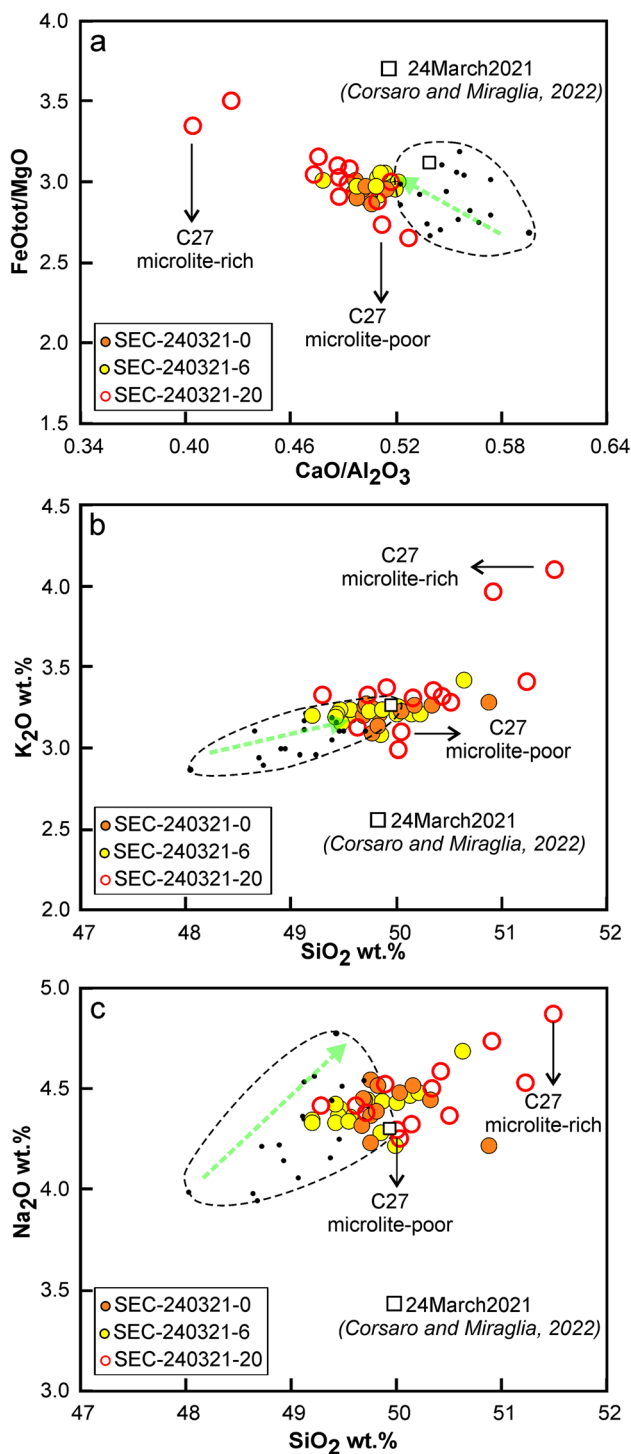


**Fig. 11** Binary plots of selected major elements and ratios in ground-mass glasses from studied samples. As comparison, we also report the variation field (dashed curve) of Corsaro and Miraglia (2022) for the entire lava fountain activity that occurred at Etna between February and April 2021, with emphasis on their sample of 24 March 2021 (white square). The green arrows are also from Corsaro and Miraglia (2022), showing the fractional crystallization paths

rim yielding  $Fo_{77}$  values. In all studied samples, composition of clinopyroxene ranges from  $Fs_{13}$  to  $Fs_{19}$  (Table S5).

### Numerical simulations of the volcanic plume dispersal in the atmosphere and on the ground

In Table S1, we reported the PLUME-MoM-TSM/HYSPLIT inputs, both those derived from real-time observations and tephra measurements and those constrained by literature review (e.g. the mixture temperature at the vent; Aubry et al. 2021). The meteorological data used to perform the simulations comes from the ERA5 global reanalysis dataset (Hersbach et al. 2020) and has been refined using the Weather Research and Forecasting (WRF) Model (Powers et al. 2017) to obtain a horizontal grid resolution of 1 km (the original ERA5 resolution is 31 km). The input parameter used to initialize PLUME-MoM-TSM was the height of the eruption column, while mass flow rate was retrieved by the model with an inversion procedure. It is worth noting that since PLUME-MoM-TSM is a wind-affected model, the mass flow rate can vary not only because of variations in column height, but also because of variations in atmospheric conditions. With this approach, the total erupted mass is an outcome of the model, and its value can be compared with the value of total erupted mass obtained by the deposit (not directly used in the simulations) to validate the numerical results. For the 23–24 March 2021 episode, the height of the eruption column appears to be well constrained at the beginning and at/near the end of the eruption episode (i.e. at 23:00 UTC on 23 March 2021 and at 11:00 UTC on 24 March 2021). Indeed, from satellite- and ground-based observations, a column of 4500 m a.s.l. (i.e. ~ 1200 m above vent level, hereafter a.v.l.) was estimated for the first 2 h (from 23:00 UTC on 23 March to 01:00 UTC on 24 March) and the last 5 h (from 06:00 UTC to 10:00 UTC on 24 March) of the eruption. The most intense explosive phase occurred between 01:00 and 06:00 UTC on 24 March, but the lack of observations due to the night and the unfavourable weather conditions made it difficult to properly estimate the maximum column height and when this maximum was attained. For this reason, we applied the optimization procedure with the aim of retrieving the values of column height from 01:00 to 06:00 UTC on 24 March, while we fixed the column to 4500 m a.s.l. for the remaining hours. To better reproduce the possible variation of the eruption column with time, we defined a three-parameter function whose output is the value of column height in the investigated time interval discretized in time slots of 30 min (i.e. we considered 10 values of column height covering a total of 5 h) (Fig. S6). The parameters of the function are named *Skew* (asymmetry of the function), *Flat* (flatness of the function) and  $\Delta h$  (maximum deviation from a reference value  $h_{ref}$  indicating the neutral buoyancy height a.v.l.) and allow us to describe a unimodal

temporal variation of the column height. In the optimization, the searching intervals for the three parameters were set as  $[-0.9; 0.9]$  for *Skew*,  $[103; 102]$  for *Flat* and  $[100; 2400]$  for  $\Delta h$  (with  $h_{\text{ref}} = 800$  m). A detailed description of the function can be found in the [Appendix](#).

We performed a total of 1000 evaluations (i.e. 1000 PLUME-MoM-TSM/HYSPLIT simulations) in order to find the temporal evolution of the eruption column height that would best reproduce the observed deposit, and the retrieved optimum values for the parameters are as follows:  $Skew = -0.04$ ,  $Flat = 10^{-3}$  and  $\Delta h = 1544$  m. From the numerical results (Fig. S7), it appears that from 01:00 to 02:30, column height remains stable at 4500 m a.s.l. (1200 m a.v.l.). The maximum height is reached between 03:00 and 03:30 with a value of 6440 m a.s.l. (3140 m a.v.l.). From 03:30, it decreases to 4750 m a.s.l. (1200 m a.v.l.), and from 04:00 to 06:00, it remains stable at 4500 m a.s.l. We set a constant height of 4500 m a.s.l. for the hours not included in the optimization.

Assuming the column height time series described above, Fig. 12a shows the simulated tephra deposit of the 23–24 March 2021 episode. From the results of PLUME-MoM-TSM, the mass flow rate corresponding to the estimated column heights varies from  $1.23 \times 10^4$  kg/s at 23:00 UTC, reaches a maximum at  $1.96 \times 10^5$  kg/s between 03:00 and 03:30 UTC, and then returns to low values, being equal to

$8.18 \times 10^3$  kg/s at 11:00 UTC. This results in a simulated total erupted mass of  $6.76 \times 10^8$  kg. In the proximal deposit (up to 10 km from the vent), we found ground loadings of  $\sim 10$  kg/m<sup>2</sup>, while those of 0.01 kg/m<sup>2</sup> are found in the distal zones (up to 40 km from the vent). As shown in Fig. 12b, the simulated ground loadings at the 34 sampling locations fit well with the field measured ones. Indeed, the majority of the simulated loadings differed from the observed ones by factor 5(1/5). The remaining loadings are within one order of magnitude from the observed ones, and only five points are slightly outside. A particularly good agreement between the observed and the simulated loads emerges for the points of the proximal deposit (red dots in Fig. 12 corresponding to observed loads between 1 and 10 kg/m<sup>2</sup>). We highlight that the evolutionary algorithm used in the optimization tries to minimize the optimization function by sampling the complete parameter space. Thus, multiple optimal solutions can result from this analysis (i.e. simulations leading to similar values of the optimization function). However, by checking the simulations giving the best-fitting results, we found for all of them similar trends in the evolution of the column height during the investigated hours (the maximum height is always about 6500 m a.s.l. and the most intense activity lasts less than 1 h). Thus, the numerical solution that we present appears to be robust with respect to the parameter space considered.

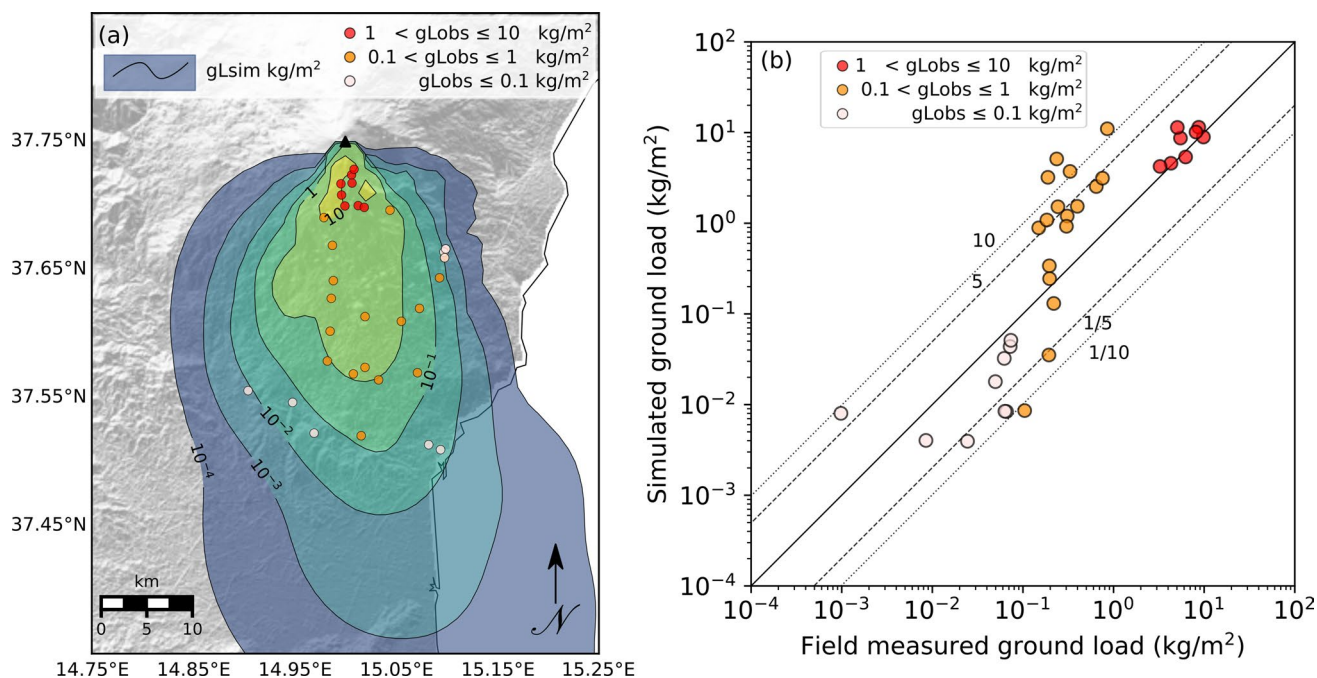


**Fig. 12** **a** Tephra ground deposit of the 23–24 March 2021 episode resulting from the best-fitting PLUME-MoM-TSM/HYSPLIT simulation (gLsim). Coloured dots indicate the sampling locations of the ground loadings (gLobs) used to perform the optimization. **b** Comparison between the simulated and observed ground loadings for the

best-fitting simulation. The continuous black line indicates a perfect match between simulated and observed values, while dashed and dotted lines indicate differences of factors 5(1/5) and 10(1/10), respectively

## Discussion

### Relationships between tremor pattern, eruption styles and tephra fallout deposits

In the world, several basaltic systems have shown in the recent past and still show an episodic eruptive behaviour in terms of Strombolian activity, lava fountains or paroxysmal episodes, e.g. Kīlauea, Hawaii, USA (Swanson et al. 1979; Mueller et al. 2018); Piton de la Fournaise, La Reunion Island, France (Thivet et al. 2020a, 2020b); and Villarrica, Chile (Romero et al. 2018). The specificity of Etna, when compared to similar mafic systems, is the intensity of the explosive activity that results in magma jets several hundred meters high and eruption columns up to more than 10 km high, associated with volcanic plumes and tephra fallouts extending tens to hundreds of km away from the volcano (Andronico et al. 2021a and references therein). Moreover, this cyclic feature has certainly reached its maximum expression and also predictability at Etna (D'Agostino et al. 2013), where hundreds of paroxysmal episodes over the past 30 years have provided a wealth of information on explosive volcanic processes. Here, each episode has unique characteristics, and their analysis through multidisciplinary investigations and the integration of the obtained results can significantly advance our understanding of these processes. At the same time, the paroxysmal activity from Etna can properly be compared to other mafic volcanoes to evaluate differences and common features, thus improving the hazard assessment of the basaltic explosive volcanism.

The 23–24 March 2021 lava fountain, which is also the penultimate episode of the February–April sequence, together with the last episode of 31 March–1 April 2021, were longer (13.5 h and 14.8 h, respectively) and with longer time interval (~ 5 days and > 7 days, respectively) between consecutive episodes than before. This unusual evolution of eruptive activity compared to previous episodes is also evident from the overlap of the tremor patterns of all the 17 episodes occurring from 1 February to 1 April 2021 (Fig. 2c). The temporal evolution of the tremor amplitude of the 23–24 March episode is, in fact, ‘flattened’ on the tremor values ( $y$ -axis), reflecting well both the slower increase and decrease of the eruptive phenomena than the other 16 episodes. An almost regular time interval with an average time interval of only 2.2 days (Fig. 2a; Andronico et al. 2021a) recurred for the previous 15 lava fountains, matching the episodes of volcanic tremor increasing, and consistently (at Etna and not only) with a fairly regular, ‘cyclic’ collapse of a foam layer formed by the bubble accumulation in the upper portion of the magma chamber (Jaupart and Vergnolle 1988, 1989;

Vergnolle and Jaupart 1990; Vergnolle 1996, 2008; Allard et al. 2005; Vergnolle and Gaudemer 2012). The collapsing foam model was also proposed for Villarrica during the March 2015 eruption, a short-lived, large-scale lava fountain triggered by a rejuvenated, volatile-rich magmatic intrusion (Romero et al. 2018). Recently, Thivet et al. (2020a) showed that also Piton de la Fournaise is characterized by simple patterns of rapid exponential decay in magma output rates (Harris et al. 2007), emplacing small volumes of lava ( $< 10 \times 10^6 \text{ m}^3$ ) during each eruptive episode with similar characteristics in terms of duration, eruption pattern and total extruded volume.

However, Andronico et al. (2021a) recommended that an alternative model could effectively be invoked for ‘transitional’ eruptions that exhibit both Strombolian and Hawaiian styles during the paroxysmal phase, which are often dominant during the last episodes of several past sequences of paroxysms at Etna and also characterized by an increasing time interval associated with a slower increase of the tremor pattern.

We therefore suggest that transitional activities, like the 23–24 March 2021 episode, can be related to a different process of magma ascent in the conduit dominated by a rapid volatile exsolution. This is the ‘rise speed dependent’ model (Parfitt 2004; Parfitt and Wilson 1995), an alternative to the ‘bubble foam’ model. This is well supported by the lower column height (a proxy for the eruption intensity) and less powerful fountaining activity of the 23–24 March compared to the previous 2021 paroxysmal episodes, which were characterized by a sharp, impulsive tremor increase during the resumption phase (Andronico et al. 2021a; Fig. 2a). A similar eruptive mechanism, consisting of a discontinuous flow of gas slugs, is thought to accompany the Strombolian phases towards the end of lava fountaining activity at Piton de la Fournaise (Thivet et al. 2020a).

Additionally, earlier and faster episodes were apparently less energetic in terms of maximum tremor amplitude (Fig. 2a), but much more intense in terms of mass loading per square meter than the 23–24 March episode. For example, on 16 February (1st episode), 28 February (7th) and 4 March (9th), we measured from 2 to 4 more amounts of tephra ( $461\text{--}922 \text{ g/m}^2$ ) at 15–16.3 km of distance from the SEC (Pardini et al. 2023) compared to sample SEC-240321–9 ( $243 \text{ g/m}^2$ ), collected at a similar distance (16.2 km) along the dispersal axis on 24 March. This further suggests that the 23–24 March episode had a lower intensity, at least compared to the three episodes referred to, not only in terms of mass loading but even more of mass eruption rate.

The bimodality of the 23–24 March total grain size distribution supports the importance of the conclusive phase in terms of both the quantity of ash and the duration of its emission, resulting in a larger amount of fine-grained tephra

able to affect the tail of the total grain size distribution of the total deposit than how it occurred during previous paroxysmal episodes at Etna, which did not show a bimodal pattern in the tephra fallout deposit (at least among those published; i.e. Andronico et al. 2009, 2014a, 2014b; Edward et al. 2018). On the other hand, the lack of bimodality in the grain size patterns of individual samples is a clear indication of the absence of coeval size-selected sedimentary processes, as occurred, for example, in September 2016 at Piton de la Fournaise, where two vents with different activities (Hawaiian fountaining and transient explosive activity) were simultaneously active (Thivet et al. 2020b). On the other hand, on 24 March at Etna, the dispersal and sedimentation of tephra were subjected to similar processes of wind transport and settling of particles for all samples, which followed each other and were only affected by the variation in height of the eruption column from the paroxysmal to the conclusive phase. This proves that the eruption of finer particles during a relatively long-lasting conclusive phase (~6 h of mostly prolonged ash emissions), with a clearly lower mass eruption rate than the paroxysmal phase (dominated by lava fountaining), may mislead the estimation of the effective physical parameters of the fallout deposit. Due consideration should therefore be applied when assessing the real-time volcanic hazard of tephra dispersal (Pardini et al. 2023).

Further considerations on the tephra fallout deposit (total and partial ground load) that also support the discrimination of tephra deposition during the paroxysmal phase from that of the conclusive phase, together with an evaluation of the tephra impact during the episode, are undertaken in the section ‘Numerical modelling and implications for hazard assessment’.

### A comprehensive model for magma degassing processes and eruption dynamics

Following the time correlation of a lava fountain with the gas-phase composition is crucial for drawing the magma-degassing dynamic, responsible for the eruption style and the shift between eruption styles during the three main phases (resumption, paroxysmal and conclusive).

Results of VSD in clasts from the 23–24 March 2021 episode indicate how the paroxysmal phase was mainly characterized by highly vesicular fragments (55–80 vol%; 60 vol% on average), with  $N_v$  between  $10^2$  and  $10^4$  mm<sup>-3</sup>, characterized by round and poorly connected vesicles of about 150 μm in diameter. On the other hand, the low amount of juvenile material erupted during the conclusive phase has a lower degree of vesicularity (20–55 vol%; 45 vol% on average), associated with lower  $N_v$  ( $10^2$ – $10^3$  mm<sup>-3</sup>) and larger vesicles (200 μm) than the paroxysmal one (Fig. 9a–c). These results are in agreement with previous studies on the juvenile scoriae discharged by Etna (Polacci et al. 2006).

Furthermore, when compared with a compilation of textural data from literature (Colombier et al. 2021), in the diagram  $N_v$  vs vesicularity, most of the products emitted during the paroxysmal phase fall in the field of the Hawaiian style, while in a log–log plot of  $N_v > L$  (mm<sup>-3</sup>) vs bubble diameter ( $L$ ; mm), the VSD fits well ( $R^2 = 0.99$ ) with exponential trends (Fig. S8a–c). These features can be acquired during at least three events of bubble nucleation and growth (Blower 2001; Blower et al. 2003; Shea et al. 2010), resulting in the formation of a foam layer at the top of a magmatic reservoir.

In this framework, the magma degassing, partly dominated by a bubbly flow, is characterized by the coupling of bubbles with the magma, triggering its acceleration to the surface and the inertial fragmentation during sustained lava-fountaining (Namiki and Manga 2008; Houghton et al. 2021; La Spina et al. 2021). The occurrence of protruding tips on the edge of ash fragments is a further suggestion of the inertial fragmentation of a low-viscosity, high-temperature magma. The measured differences in the VSD (Fig. 9c and Fig. S8a–c) between the proximal and distal samples related to the paroxysmal phase can be an effect of bubble coalescence, due to post-fragmentation vesiculation of large clasts, or interior of transitional rim-to-core clasts (Stovall et al. 2011, 2012; Porritt et al. 2012), which undergo refragmentation in air-producing ash that can also travel far from the vent.

In the diagram  $N_v$  vs vesicularity (Fig. 9b), most of the coarse ash from the conclusive phase falls in the field of submarine/Strombolian eruptions (Colombier et al. 2021), and in the log–log  $N_v (> L)$  vs  $L$  plot, VSD is described as an exponential distribution ( $R^2 = 0.99$ ) for the bubbles smaller than 170 μm and as a power-law distribution with exponent 3.8 ( $R^2 = 0.99$ ) for the largest bubbles (Fig. S8d). These features can be attributed to bubble coalescence, where large bubbles ascend faster than surrounding bubbles and can absorb the small bubbles as they rise, causing slug dynamics and deep Strombolian activity. This regime of degassing can be favoured by a decrease in magma ascent rate and the shifting in melt viscosity due to cooling, degassing and crystallization of the involved magma. Evidence of this is also the large amount of ash production and the high values of CVX and SLD of their morphology (Fig. 8).

The retrieval of solar FTIR measurements, performed on the morning of 24 March, allowed us to trace the temporal evolution (every 8 s) of the gas phase, in terms of SO<sub>2</sub> and HCl, in the conclusive phase of the eruption, i.e. when both seismic tremor and either eruptive activity dropped gradually (Fig. 13). The SO<sub>2</sub>/HCl ratio shows a decreasing trend from 8 to 2. Moreover, the regularly spaced peaks with high amounts of gas, which characterize the overall trend, can be interpreted as the occurrence on the surface of explosions resembling Strombolian activity/episodes (SA/SE eruption types of Andronico et al. 2021a). Recent studies testify that

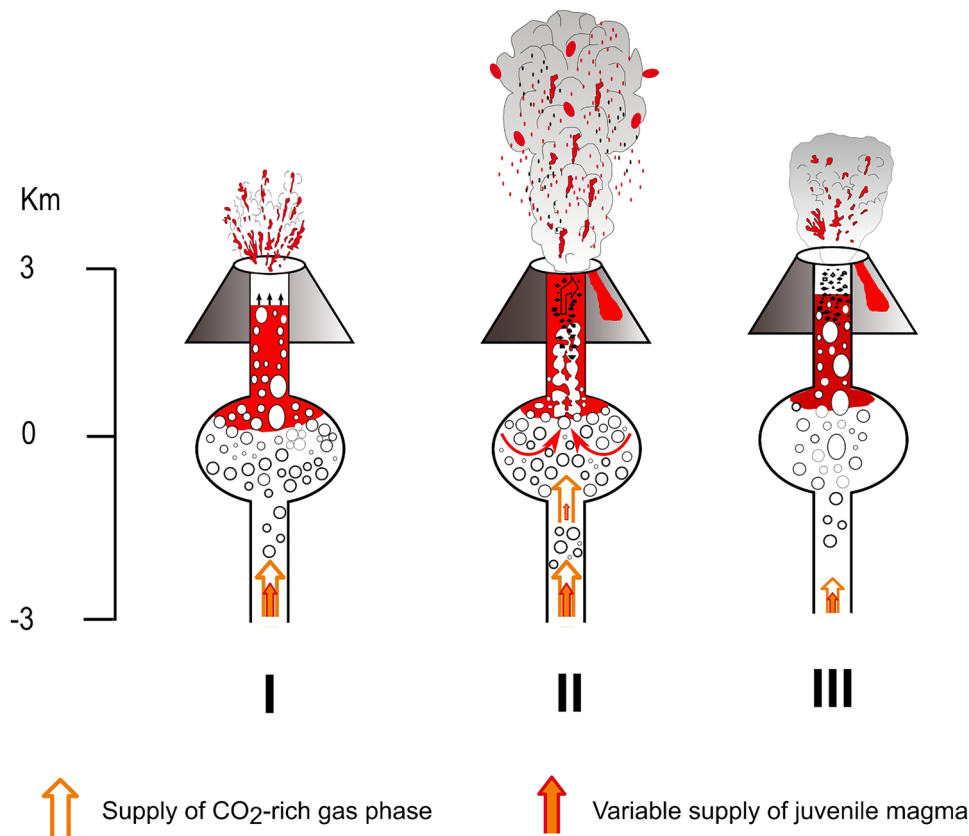


**Fig. 13** Interpretative model of the plumbing system proposed for the studied lava fountain. (I) Resumption phase: the level of residual magma rises in the conduit due to the development of a foam level triggered by the arrival of a new input of gas-rich magma in the magma chamber. The bubble coalescence is increasing, and large bubbles ascend the conduit, thus yielding Strombolian activity promoting rise of magma level inside the conduit. The higher level of magma produces lava output and gradually induces a more vigorous coalescence process with growing Strombolian activity and increase

of tremor signal. (II) Paroxysmal phase: true lava fountaining or closely timed powerful Strombolian explosions occurred. The continuous emptying of the conduit triggers the collapse of the foam, which rises within the conduit. At the fragmentation level, the mixture is constituted essentially of gas (e.g. 90% gas and 10% melt). During this phase, the seismic tremor reaches its maximum amplitude. (III) Conclusive phase: both seismic tremor and eruptive activity dropped either gradually or rapidly

the paroxysmal activity of the SEC is driven by a gas phase ( $\text{CO}_2$  richer) with high  $\text{SO}_2/\text{HCl}$  ratio ( $\geq 10$ ), previously accumulated in a foam layer 2 km below the top (Allard et al. 2005; La Spina et al. 2015; Aiuppa et al. 2017). The decreasing trend observed in  $\text{SO}_2/\text{HCl}$  ratio during the last part of the studied episode indicates a progressive decrease in the rate of ascent of gas bubbles with respect to the paroxysmal phase. Ascending at a slower rate (possibly due to a decrease in magma ascent rate), the bubbles have more time to re-equilibrate with the surrounding melt, grow and coalesce, suggesting a much shallower gas equilibrium due to a syn-eruptive halogen (HCl) degassing process which results in the formation of larger vesicles.

It is commonly assumed that annular flow characterizes lava fountain activity while slug flow corresponds to the discrete bursts typical of Strombolian activity (e.g. Vergnolle and Jaupart 1986; Seyfried and Freundt 2000; Pioli et al. 2012; Fig. 13). Therefore, the occurrence of bursts of

isolated bigger bubbles is testified by a higher amount of retrieved gas. All these differences can be attributed to a decrease in both gas flow and magma ascent rates during the eruption, passing from a sustained annular flow (paroxysmal phase) to an intermittent dynamic of gas slugs within the conduits (conclusive phase) (Carbone et al. 2015).

As previously reported, a common lava fountaining episode on Etna has been divided into three main phases (Alparone et al. 2003; La Spina et al. 2015). However, in terms of eruption style, the 23–24 March episode differed from previous episodes in several ways, as also suggested from the tremor data (Andronico et al. 2021a; Fig. 2). Figure 13 shows the interpretative model of the plumbing system proposed for the studied lava fountain in light of what has been said so far. In detail, the resumption phase (I) was characterized by a long period of ascending tremor associated with increasing (in both intensity and frequency) Strombolian explosions up to sustained lava fountains. The

formation of an evident effusive activity was unusually not observed, unlike what happens during most of the fountain episodes (Alparone et al. 2003) as well in the previous ones that occurred in 2021. Again, the paroxysmal phase (II) had less powerful fountaining activity and eruption plume height than the previous 15 episodes of the 2021 sequence, and indeed only about halfway through the paroxysmal phase, an efficient effusive activity began. Finally, the start of the conclusive phase (III) did not reflect a sharp decline of the paroxysmal activity as usual, but a period of lower-intensity, probably deep, Strombolian explosive activity, associated with an unusual, prolonged ash emission forming a bent, poor-fed eruption plume.

### Indications from petrological and textural analyses

The large compositional dataset obtained in this study on about 40 ash fragments, together with a significant amount of data on vesicularity, componentry, morphology and shape parameters of ash particles, allowed us to investigate the syn-eruptive processes associated with the 23–24 March 2021 explosive event, also grasping the mechanisms leading to the transition from the paroxysmal to the conclusive phase.

The core-to-rim composition of olivine phenocrysts can provide insights into the source zone/s of the magma that fed the eruption (Kahl et al. 2015). The presence of cores with composition  $Fo_{82}$  in olivine from the paroxysmal phase indicates that the deep reservoir identified at depths between 6 and 10 km (Spilliaert et al. 2006; Kahl et al. 2015; Corsaro and Miraglia 2022) was no longer active during the studied event. The statistically most probable deeper magma ponding zone can be identified at depths of 5–6 km, where the rims of olivine  $Fo_{72-78}$  crystallize. During its ascent, the deep-sourced magma intercepts the reservoir identified at about 1.5–2 km below the SEC (Andronico and Corsaro 2011; La Spina et al. 2015; De Gori et al. 2021), where the composition of the rims of olivine reaches  $Fo_{71}$ . This trend is also confirmed by the composition of the residual glasses which present a very wide range of variability, from compositions that overlap those of the fountains of the previous weeks (early March), up to more evolved compositions than those defined by Corsaro and Miraglia (2022) for the 23–24 March 2021 episode, because we also analysed fragments with microlite content  $> 15\%$ . In general, the variability in the residual glass composition is attributed to the superposition of the magma mixing between the two identified ponding zones and to the fractional crystallization of olivine, plagioclase and pyroxene, as already previously suggested by Corsaro and Miraglia (2022). The persistence of a limited supply of magma from the reservoir located at 5–6 km not only during the paroxysmal phase of the 23–24 March lava fountain, but also during its conclusive phase, is evidenced

by the presence, in the SEC-240321–20 sample, of reverse zoned olivine phenocrysts with core  $Fo_{65}$ , rimmed by  $Fo_{71-77}$  composition. Furthermore, in this sample, we also identified the mingling texture between glasses of different compositions (Fig. 10f), which confirms that the contribution of the magma located at a depth of 5–6 km was active during the whole event. However, in the conclusive phase of the eruption, we note the abundance of glasses with microlite content  $> 20\%$  and residual glasses with  $CaO/Al_2O_3 < 0.49$ , indicating values of crystallinity higher than in samples from the paroxysmal phase. These features are indicative of a magma that evolves by crystallization, in the more superficial portions of the system. Moreover, the number of bubbles per volume ( $N_v$ ) can be used to constrain the magma decompression rates, and hence the magma ascent velocity within the conduit (Toramaru 1995, 2006). The  $N_v$  values obtained in this study, in fact, fall in the same range of those obtained in paroxysms with similar intensity at other basaltic volcanoes (e.g. Stromboli; Andronico et al. 2021a; Pichavant et al. 2022). Our results indicate that the paroxysmal phase of the eruption shows a slightly higher  $N_v$  value compared to the conclusive phase, suggesting a gradual decrease in the magma ascent velocity over the course of the eruption rather than an abrupt end. In the light of these findings (lowest vesicularity and highest crystallinity values in sample SEC-240321–20), we suggest that the shifting towards the conclusive phase was related to a slow decrease in magma supply from the depth reservoir (in agreement with the model proposed in Fig. 13) associated with cooling, degassing and crystallization of the magma in the shallow plumbing system. This is also confirmed by the inverse relationship between the vesicularity of the groundmass and the crystal content of erupted ash (Fig. 9d). As already proposed by Polacci et al. (2019), the variations of the magma mass flow rate in the volcanic conduit can be responsible for the different mechanisms of ash generation. Thus, on the basis of petrological and textural evidence, we propose that the final phase of the eruption was fed by a more viscous, colder and more evolved magma, that resided long enough to cool, crystallize and degas, developing a network of interconnected vesicles and increasing magma permeability, which possibly generated pathways of passive or mildly explosive gas separation. Finally, the prolonged waning phase of the 23–24 March lava fountain can be interpreted as a low-energy explosive activity in which the ash recycling is favoured, and the ash generation was enhanced by the brittle behaviour of the viscous magma still residing in the conduit (D’Orlando et al. 2022). The formation of a degassed and crystallized plug at the top of the magma column was also invoked by Taddeucci et al. (2004) to explain the transition from Strombolian to ash explosions during the 2001 Etna eruption when marked by a decrease in the eruption rate, and may also occur on other basaltic volcanoes. At Piton de la Fournaise, during the

2016 eruption, a syn-eruptive degassing–driven crystallization would have enhanced the formation of a cooling magma plug and therefore the onset of transitional activity, characterized by ash emissions with the eruption of recycling material and tachylite ash particles, as well as the bimodal grain size and component pattern of the erupted tephra, considered a secondary effect due to the late change in magma supply and viscosity (Thivet et al. 2020b, c).

As a striking result of this different explosive activities in terms of eruptive dynamics and intensity, samples collected at ~27–28 km from the vent and related to the fountaining phase (SEC-240321–0 and SEC-240321–1) have similar sorting and mode to the sample collected at Fleri, i.e. at only ~13 km, and related to the last hours of activity, with the first two entirely composed by juvenile particles, while the latter containing a high percentage of recycled and lithic clasts.

### Numerical modelling and implications for hazard assessment

The numerical simulations allowed us to better understand the atmospheric transport processes of the tephra particles released during the studied episode and to further explore the characteristics of the tephra deposit.

Numerical results confirm that the anticlockwise rotation of the wind field enables distinguishing the deposit formed by the tephra particles emitted during the paroxysmal phase from that associated with the tephra particles emitted during the conclusive phase. Indeed, considering the locations of Table 1, it appears that for the sampling sites located along the dominant dispersal axis (S to SSW of the SEC), the final value of the ground load is reached before the beginning of

the conclusive phase (05:00 UTC), indicating that only the particles emitted during the paroxysmal phase contributed to the fallout. This is shown in Fig. 14a, where we report the accumulation of tephra as a function of time calculated numerically for a location positioned on the dispersal axis (Nicolosi INGV-OE). For this location, we found that the final value of the ground load is reached before 05:00 UTC. In particular, tephra particles deposited from 03:00 to 03:30 UTC, namely the time interval when the eruption column reached the maximum height. From 05:00 UTC, the ground load does not increase although tephra emission is still ongoing. This is because of the anticlockwise rotation of the wind field that moved particle deposition towards SE. On the contrary, for the location Post-Case del Vescovo (Fig. 14b), it appears that the tephra particles emitted during the conclusive phase contribute to 94% of the final ground load of 3.20 kg/m<sup>2</sup>, while a modest contribution (6% of the final ground load) derives from the particles emitted during the paroxysmal phase.

The temporal evolution of the column height retrieved by the inversion procedure is in agreement with the information on column height coming from the Volcano Observatory Notice for Aviation (VONA) messages issued during the event and available at INGV-OE website (<https://www.ct.ingv.it/index.php/monitoraggio-e-sorveglianza/prodotti-del-monitoraggio/comunicati-vona>; Corradini et al. 2018; Scollo et al. 2019; INGV-OE 2021). In particular, of the six VONAs released by the INGV-OE during the 23–24 March episode, only two contain information on the column height: the VONA issued at 03:45 UTC on 24 March contains an estimated column height of 6 km, and the VONA issued at 07:21 UTC the same day reports a column height value of 4.5 km. This temporal evolution fits well with the estimates

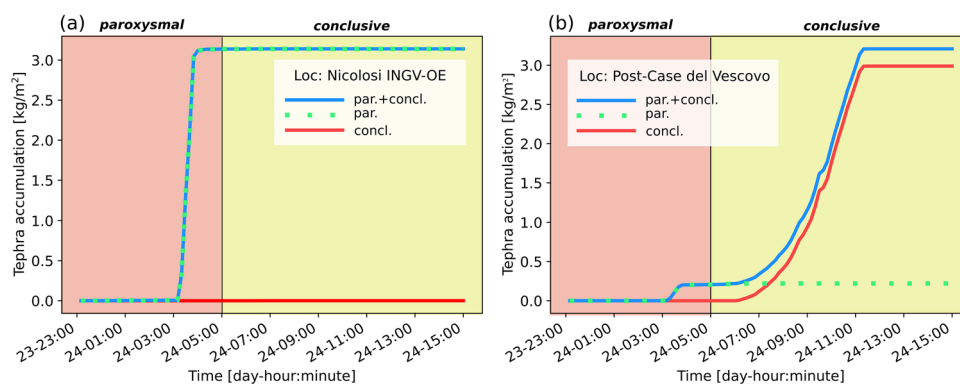


**Fig. 14** Tephra accumulation on the ground in kg/m<sup>2</sup> as a function of time in UTC for two locations of Table 1. Panel **a** refers to Nicolosi INGV-OE which is located on the main dispersal axis (S of SEC), while panel **b** is for Post-Case del Vescovo, which is located lateral to the main dispersal axis (SE of the SEC). Blue lines (par. +concl.) indicate the temporal evolution of the accumulation of tephra on the ground considering the tephra particles emitted during both the par-

oxysmal phase and the conclusive phase. Green dotted lines (par.) show the same quantity but for the particles emitted during the paroxysmal phase only (from 23:00 until 05:00 UTC). Finally, red lines (concl.) show tephra accumulation considering the tephra particles emitted during the conclusive phase (from 05:00 to 11:00 UTC). Note that the temporal evolution of the eruption column leading to these results is the one produced by the inversion procedure

produced by the numerical models, with a maximum value of column height of 6.44 km a.s.l. reached between 03:00 and 03:30 UTC on 24 March.

We can also observe that the numerically retrieved total erupted mass ( $6.67 \times 10^8$  kg) is in agreement with that derived from the deposit ( $8.03 \pm 2.38 \times 10^8$  kg) and note again that the deposit-based total erupted mass was not used to initialize the simulations. From the results of the simulations, we are able to calculate the portion of total erupted mass produced by the paroxysmal phase ( $5.40 \times 10^8$  kg erupted from 23:00 to 05:00 UTC) and that produced by the conclusive phase ( $1.36 \times 10^8$  kg erupted from 05:00 to 11:00 UTC).

Moreover, our findings have major implications in terms of hazard assessment, showing that  $3.43 \times 10^8$  kg of material was erupted from 03:00 to 03:30 UTC (i.e. when the eruption column reached the maximum height of 6.44 km a.s.l.). In fact, despite the long duration of tephra emission (12 h), it was found that 50% of total erupted mass was produced by tephra particles emitted in 30 min. This outcome reflects the temporal evolution of the mass eruption rate as resulting from the inversion procedure. Indeed, from the simulation results, the mass eruption rate producing the material erupted from 03:00 to 03:30 UTC on 24 March is  $1.96 \times 10^5$  kg/s. This value, which corresponds to a column height of 6.44 km a.s.l., is about 24 times higher than the mass eruption rate calculated for the remaining 11.5 h of the eruption when column height is 4.5 km a.s.l. (mass eruption rate ranging from  $1.23 \times 10^4$  to  $8.18 \times 10^3$  kg/s and with a mean value of  $8.28 \times 10^3$  kg/s). Since we simulated 12 h of emission discretized in 24 time intervals of 30 min each, the material erupted during a time interval with a mass eruption rate equal to  $1.96 \times 10^5$  kg/s almost coincides with that erupted in 23 time intervals having a mass eruption rate equal to  $8.28 \times 10^3$  kg/s. Thus, confirming the well-known scaling model between mass eruption rate and column height based on a power-law relationship between the two (Mastin et al. 2009; Aubry et al. 2023), a small variation in column height corresponds to significant differences in mass eruption rate and, eventually, total erupted mass. This underlines the importance of reliable quantitative observations of column height to initialize the numerical models used to forecast the dispersion and deposition patterns of tephra particles at Etna but also on other volcanoes.

## Conclusions

Lava fountains are the most common explosive eruptions in the recent eruptive history of Etna. The high variability in intensity (mass eruption rate), magnitude (total mass; only tephra products) and duration of an entire single episode, as well as individual eruptive phases (resumption, paroxysmal,

conclusive), is worthy of consideration to improve the knowledge of the ongoing eruptive processes. In this work, we have presented a multidisciplinary approach to examine a single episode that first includes video recordings from surveillance cameras, seismic tremor signal, gas plume geochemistry and fieldwork, then focuses on a thorough study of the tephra fallout deposit and the erupted products (grain size, shape, petrological and compositional analyses), and lastly assesses the numerical modelling of the eruptive source parameters.

We have shown that seismic tremor and video-camera recordings during the fluctuations of the explosive phases match well with changes in the height of the eruption column. What we have learned and better quantified than previous studies on lava fountains is that tephra erupted can have petro-textural characteristics which are expected to vary with the escalation or waning of the explosive activity. Unlike almost all the previously studied episodes, the anti-clockwise rotation of the volcanic plume after 05:00 UTC prevented the mixing of the tephra fallen to the ground during the paroxysmal and conclusive phases. At the same time, it also favoured the partial physical separation of the erupted products and thus the recognition of the clasts related to the prolonged conclusive phase, although characterized by a minor amount of tephra discharge compared to the paroxysmal phase. Supported by this evidence, we were able to interpret pre- and syn-eruptive processes by correlating measurements of the gas phase in the volcanic plume (in terms of  $\text{SO}_2$  and HCl) with textural and petro-compositional results on erupted products, proposing a simple model of the plumbing system for the studied lava fountain, which provides lava flow output only from the paroxysmal phase onwards.

In addition, the total erupted mass obtained from an accurate reconstruction of the 23–24 March fallout deposit was used to validate very close numerical simulations (30-min time steps) of the volcanic column and of the tephra deposition, providing valuable insights into the dynamics of lava fountaining at Etna. By reproducing the temporal impact of tephra load and dispersal around the volcano as closely as possible to the observed deposit, the implications of the numerical modelling are in fact relevant in terms of volcanic hazard, indicating that half of tephra mass was erupted between 3:00 and 3:30 UTC of 24 March, i.e. in less than 3% of the total duration of the entire episode (17 h).

Our study therefore shows that lava fountains of relatively low intensity (such as the 23–24 March 2021 episode) are able to cause not only prolonged hazards in the atmosphere, but also significant impact of tephra fallout on the ground, which in the studied case would occur in just a few tens of minutes despite the lengthy duration of the episode. This information can help better understand the potential land damage from tephra fallout and improve hazard assessment



and mitigation strategies, especially for much more intense fountaining episodes than the 23–24 March one.

For the future, this work also highlights that separating tephra falling during a lava fountain on some key, proximal to distal sites around Etna at established time intervals, e.g. 30 min each, could be useful to better interpret the eruptive processes that precede, accompany and follow the paroxysmal phase of each episode, and ultimately to better address the forecasting of volcanic plumes.

## Appendix

### Function for the characterization of the column height

We defined a three-parameter function ( $h$ ) to describe the unimodal distribution of the height of the eruptive column during the most intense phase of the eruption. The three parameters describe the asymmetry of the distribution (*Skew*), the flatness (*Flat*) and the maximum deviation with respect to a reference value ( $\Delta h$ ).

The function  $h$  is

$$h = h_{\text{ref}} + \Delta h \left( \frac{h_{\text{temp}}}{H_{\text{temp}}} \right)^{\frac{1}{\text{Flat}}}$$

where  $h_{\text{ref}}$  is a term indicating a reference value of column height, and  $h_{\text{temp}}$  is

$$h_{\text{temp}} = \frac{1}{\sqrt{2\pi}} e^{-\frac{1}{2}x^2}$$

and  $H_{\text{temp}}$  is the maximum value of  $h_{\text{temp}}$ .

The variable  $x$  of  $h_{\text{temp}}$  is defined as

$$x = x_0^{1-\text{Skew} \cdot 2.0 - 1.0}, \text{Skew} > 0$$

$$x = 1.0 - (1.0 - x_0)^{1+\text{Skew} \cdot 2.0 - 1.0}, \text{Skew} \leq 0$$

where  $x_0$  assume values in the interval (0,1).

**Supplementary Information** The online version contains supplementary material available at <https://doi.org/10.1007/s00445-024-01745-5>.

**Acknowledgements** We especially wish to thank L. Messina, E. Maiolino and G. Suriani for providing a few tephra samples, and L. Messina for her full-time availability in the INGV-OE laboratories. P. Montalto is thanked for helping in retrieving the videos of the 24 March 2021 paroxysm. We thank the Associate Editor Prof. S. Vergnolle, Dr. J. E. Romero and an anonymous reviewer for their constructive comments and suggestions upon reviewing the manuscript. We are also very much indebted to the INGV-OE staff who maintained the video-camera network with great efficiency during the 2021 paroxysmal

activity. S. Conway is thanked for significantly revising the English language.

**Funding** Open access funding provided by Istituto Nazionale di Geofisica e Vulcanologia within the CRUI-CARE Agreement.

**Open Access** This article is licensed under a Creative Commons Attribution 4.0 International License, which permits use, sharing, adaptation, distribution and reproduction in any medium or format, as long as you give appropriate credit to the original author(s) and the source, provide a link to the Creative Commons licence, and indicate if changes were made. The images or other third party material in this article are included in the article's Creative Commons licence, unless indicated otherwise in a credit line to the material. If material is not included in the article's Creative Commons licence and your intended use is not permitted by statutory regulation or exceeds the permitted use, you will need to obtain permission directly from the copyright holder. To view a copy of this licence, visit <http://creativecommons.org/licenses/by/4.0/>.

## References

- Adams BM, Ebeida MS, Eldred MS, Geraci G, Jakeman JD, Maupin KA, Monschke JA, Stephens JA, Swiler LP, Vigil DM, Wildey TM, Bohnhoff WJ, Dalbey KR, Eddy JP, Frye JR, Hooper RW, Hu KT, Hough PD, Khalil M, Ridgway EM, Winokur JG, Rushdi A (2014) Dakota, a multilevel parallel object-oriented framework for design optimization, parameter estimation, uncertainty quantification, and sensitivity analysis: version 6.8 user's manual. Sandia Technical Report SAND2014-4633 (updated May 2018)
- Aiuppa A, Bitetto M, Francoforte V, Velasquez G, Bucarey-Parra C, Giudice G, Liuzzo M, Moretti R, Moussallam Y, Peters N, Tamburello G, Valderrama OA, Curtis A (2017) A CO<sub>2</sub>-gas precursor to the March 2015 Villarrica volcano eruption. *Geochem Geophys Geosys* 18:2120–2132. <https://doi.org/10.1002/2017GC006892>
- Allard P, Burton M, Murè F (2005) Spectroscopic evidence for a lava fountain driven by previously accumulated magmatic gas. *Nature* 433:407–410. <https://doi.org/10.1038/nature03246>
- Alparone S, Andronico D, Lodato L, Sgroi T (2003) Relationship between tremor and volcanic activity during the Southeast Crater eruption on Mount Etna in early 2000. *J Geophys Res: Solid Earth* 108(B5). <https://doi.org/10.1029/2002JB001866>
- Andronico D, Corsaro RA (2011) Lava fountains during the episodic eruption of South-East Crater (Mt. Etna), 2000: insights into magma-gas dynamics within the shallow volcano plumbing system. *Bull Volcanol* 73:1165–1178. <https://doi.org/10.1007/s00445-011-0467-y>
- Andronico D, Del Carlo P (2016) PM10 measurements in urban settlements after lava fountain episodes at Mt. Etna, Italy: pilot test to assess volcanic ash hazard on human health. *Nat Hazards Earth Syst Sci* 16:29–40. <https://doi.org/10.5194/nhess-16-29-2016>
- Andronico D, Scollo S, Cristaldi A, Caruso S (2008) The 2002–03 Etna explosive activity: tephra dispersal and features of the deposit. *J Geophys Res* 113:B04209. <https://doi.org/10.1029/2007JB005126>
- Andronico D, Cristaldi A, Del Carlo P, Taddeucci J (2009) Shifting styles of basaltic explosive activity during the 2002–03 eruption of Mt. Etna. *Italy J Volcanol Geotherm Res* 180:110–122. <https://doi.org/10.1016/j.jvolgeores.2008.07.026>
- Andronico D, Scollo S, Lo Castro MD, Cristaldi A, Lodato L, Taddeucci J (2014b) Eruption dynamics and tephra dispersal from the 24 November 2006 paroxysm at South-East Crater, Mt Etna, Italy. *J Volcanol Geotherm Res* 274:78–91. <https://doi.org/10.1016/j.jvolgeores.2014.01.009>

- Andronico D, Di Roberto A, De Beni E, Behncke B, Bertagnini A, Del Carlo P, Pompilio M (2018) Pyroclastic density currents at Etna volcano, Italy: the 11 February 2014 case study. *J Volcanol Geotherm Res* 357:92–105. <https://doi.org/10.1016/j.jvolgeores.2018.04.012>
- Andronico D, Cannata A, Di Grazia G, Ferrari F (2021a) The 1986–2021 paroxysmal episodes at the summit craters of Mt. Etna: insights into volcano dynamics and hazard. *Earth-Sci Rev* 220:103686. <https://doi.org/10.1016/j.earscirev.2021.103686>
- Andronico D, Del Bello E, D’Oriano C, Landi P, Pardini F, Scarlato P, Taddeucci J, Cristaldi A, Ciancetto F, Pennacchia F (2021b) Uncovering the eruptive patterns of the 2019 double paroxysm eruption crisis of Stromboli volcano. *Nat Commun* 12(1):1–14. <https://doi.org/10.1038/s41467-021-24420-1>
- Andronico D, Scollo S, Cristaldi A, Lo Castro MD (2014a) Representativity of incompletely sampled fall deposits in estimating eruption source parameters: a test using the 12–13 January 2011 lava fountain deposit from Mt. Etna volcano, Italy. *Bull Volcanol* 76(861). <https://doi.org/10.1007/s00445-014-0861-3>
- Aubry TJ, Engwell S, Bonadonna C, Carazzo G, Scollo S, Van Eaton AR, Taylor IA, Jessop D, Eyehenne J, Gouhier M, Mastin LG, Wallace KL, Biass S, Bursik M, Grainger RG, Jellinek M, Schmidt A (2021) The independent volcanic eruption source parameter archive (IVESPA, version 1.0): a new observational database to support explosive eruptive column model validation and development. *J Volcanol Geotherm Res* 417:107295. <https://doi.org/10.1016/j.jvolgeores.2021.107295>
- Aubry TJ, Engwell SL, Bonadonna C, Mastin LG, Carazzo G, Van Eaton AR, Jessop DE, Grainger RG, Scollo S, Taylor IA, Jellinek AM (2023) New insights into the relationship between mass eruption rate and volcanic column height based on the IVESPA data set. *Geophys Res Lett* 50(14):e2022GL102633
- Barsotti S, Andronico D, Neri A, Del Carlo P, Baxter PJ, Aspinall WP, Hincks T (2010) Quantitative assessment of volcanic ash hazards for health and infrastructure at Mt. Etna (Italy) by numerical simulation. *J Volcanol Geotherm Res* 192(1–2):85–96. <https://doi.org/10.1016/j.jvolgeores.2010.02.011>
- Blott SJ, Pye K (2001) GRADISTAT: a grain size distribution and statistics package for the analysis of unconsolidated sediments. *Earth Surf Proc Land* 26(11):1237–1248
- Blower JD, Keating JP, Mader HM, Phillips JC (2001) Inferring volcanic degassing processes from vesicle size distributions. *Geophys Res Lett* 28:347–350. <https://doi.org/10.1029/2000GL012188>
- Blower JD, Keating JP, Mader HM, Phillips JC (2003) The evolution of bubble size distributions in volcanic eruptions. *J Volcanol Geotherm Res* 120. [https://doi.org/10.1016/S0377-0273\(02\)00404-3](https://doi.org/10.1016/S0377-0273(02)00404-3)
- Bonadonna C, Costa A (2012) Estimating the volume of tephra deposits: a new simple strategy. *Geology* 40:415–418. <https://doi.org/10.1130/G32769.1>
- Bonadonna C, Houghton B (2005) Total grain-size distribution and volume of tephra-fall deposits. *Bull Volcanol* 67(5):441–456. <https://doi.org/10.1007/s00445-004-0386-2>
- Burton M, Allard P, Murè F, Oppenheimer C (2003) FTIR remote sensing of fractional magma degassing at Mount Etna, Sicily. *Geol Soc Spec Publ* 213:281–293. <https://doi.org/10.1144/GSL.SP.2003.213.01.17>
- Carbone D, Zuccarello L, Messina A, Scollo S, Rymer H (2015) Balancing bulk gas accumulation and gas output before and during lava fountaining episodes at Mt. Etna. *Sci Rep* 5:18049. <https://doi.org/10.1038/srep18049>
- Cioni R, D’Oriano C, Bertagnini A (2008) Fingerprinting ash deposits of small scale eruptions by their physical and textural features. *J Volcanol Geotherm Res* 177:277–287. <https://doi.org/10.1016/j.jvolgeores.2008.06.003>
- Colombier M, Vasseur J, Houghton BF, Cáceres F, Scheu B, Kueppers U, Thivet S, Gurioli L, Montanaro C, Soldati A, Di Muro A, Dingwell DB (2021) Degassing and gas percolation in basaltic magmas. *Earth Planet Sci Lett* 573:117134. <https://doi.org/10.1016/j.epsl.2021.117134>
- Corradini S, Guerrieri L, Lombardo V, Merucci L, Musacchio M, Prestifilippo M, Scollo S, Silvestri M, Spata G, Stelitano D (2018) Proximal monitoring of the 2011–2015 Etna lava fountains using MSG-SEVIRI data. *Geosciences* 8(4):140. <https://doi.org/10.3390/geosciences8040140>
- Corsaro RA, Miraglia L (2022) Near real-time petrologic monitoring on volcanic glass to infer magmatic processes during the February–April 2021 paroxysms of the South-East Crater, Etna. *Front Earth Sci*. <https://doi.org/10.3389/feart.2022.828026>
- D’Agostino M, Di Grazia G, Ferrari F, Langer H, Messina A, Reitano D, Spampinato S (2013) Volcano monitoring and early warning on Mt. Etna, Sicily based on volcanic tremor: methods and technical aspects. In: Zobin V (ed) *Complex monitoring of volcanic activity: methods and results*, Chapter: 4. Nova Science Publishers, New York, USA, pp 53–92
- D’Oriano C, Bertagnini A, Cioni R, Pompilio M (2014) Identifying recycled ash in basaltic eruptions. *Sci Rep* 4:5851. <https://doi.org/10.1038/srep05851>
- D’Oriano C, Del Carlo P, Andronico D, Cioni R, Gabellini P, Cristaldi A, Pompilio M (2022) Syn-eruptive processes during the January–February 2019 ash-rich emissions cycle at Mt. Etna (Italy): implications for petrological monitoring of volcanic ash. *Front Earth Sci* 10:824872. <https://doi.org/10.3389/feart.2022.824872>
- De Gori P, Giampiccolo E, Cocina O, Branca S, Doglioni C, Chiarabba C (2021) Re-pressurized magma at Mt Etna, Italy, may feed eruptions for years. *Commun Earth Environ* 2:216. <https://doi.org/10.1038/s43247-021-00282-9>
- de’Michieli Vitturi M, Pardini F (2021) PLUME-MoM-TSM 100: a volcanic column and umbrella cloud spreading model. *Geosci Model Dev* 14(3):1345–1377. <https://doi.org/10.5194/gmd-14-1345-2021>
- Dominguez L, Bonadonna C, Forte P, Jarvis PA, Cioni R, Mingari L, Bran D, Panebianco JE (2020) Aeolian remobilisation of the 2011-Cordón Caulle tephra-fallout deposit: example of an important process in the life cycle of volcanic ash. *Front Earth Sci* 7:343. <https://doi.org/10.3389/feart.2019.00343>
- Edwards MJ, Pioli L, Andronico D, Scollo S, Ferrari F, Cristaldi A (2018) Shallow factors controlling the explosivity of basaltic magmas: the 17–25 May 2016 eruption of Etna Volcano (Italy). *J Volcanol Geotherm Res* 357:425–436. <https://doi.org/10.1016/j.jvolgeores.2018.05.015>
- Fierstein J, Nathenson M (1992) Another look at the calculation of fallout tephra volumes. *Bull Volcanol* 54:156–167. <https://doi.org/10.1007/BF00278005>
- Francis P, Burton MR, Oppenheimer C (1998) Remote measurement of volcanic gas compositions by solar occultation spectroscopy. *Nature* 396:567–570. <https://doi.org/10.1038/25115>
- Gill J, Michael P, Woodcock J, Dreyer B, Ramos F, Clague D, Kela J, Scott S, Konrad K, Stakes D (2016) *J Petrol* 57:863–896
- Hansen RO (1993) Interpretive gridding by anisotropic kriging. *Geophysics* 58(10):1491–1497. <https://doi.org/10.1190/1.1443363>
- Harris AJL, Dehn J, Calvari S (2007) Lava effusion rate definition and measurement: a review. *Bull Volcanol* 70(1):1–22. <https://doi.org/10.1007/s00445-007-0120-y>
- Hersbach H, Bell B, Berrisford P, Hirahara S, Horányi A, Muñoz-Sabater J, Nicolas J, Peubey C, Radu R, Schepers D, Simmons A, Soci C, Abdalla S, Abellan X, Balsamo G, Bechtold P, Biavati G, Bidlot J, Bonavita M, De Chiara G, Dahlgren P, Dee D, Diamantakis M, Dragani R, Flemming J, Forbes R, Fuentes M, Geer A, Haimberger L, Healy S, Hogan RJ, Hólm E, Janisková M, Keeley S, Laloyaux P, Lopez P, Lupu C, Radnoti G, de Rosnay P, Rozum

- I, Vamborg F, Villaume S, Thépaut J-N (2020) The ERA5 global reanalysis. *Q J R Meteorol Soc* 146(730):1999–2049. <https://doi.org/10.1002/qj.3803>
- Horwell CJ, Baxter PJ (2006) The respiratory health hazards of volcanic ash: a review for volcanic risk mitigation. *Bull Volcanol* 69:1–24. <https://doi.org/10.1007/s00445-006-0052-y>
- Houghton BF, Tisdale CM, Llewellyn EW, Taddeucci J, Orr TR, Walker BH, Patrick MR (2021) The birth of a Hawaiian fissure eruption. *J Geophys Res, Solid Earth*, e2020JB020903. <https://doi.org/10.1029/2020JB020903>
- Houghton BF, Smith RT (1993) Recycling of magmatic clasts during explosive eruptions: estimating the true juvenile content of phreatomagmatic volcanic deposits. *Bull Volcanol* 55:414–420. <https://doi.org/10.1007/BF00302001>
- INGV-OE (2021) ETNA Bollettino Settimanale 22/03/2021 - 28/03/2021. Rep. N. 13/2021. Available at <https://www.ct.ingv.it/index.php/monitoraggio-e-sorveglianza/prodotti-del-monitoraggio/bollettini-settimanali-multidisciplinari/482-bollettino-settimanale-sul-monitoraggio-vulcanico-geochimico-e-sismico-del-vulcano-etna20210330/file>
- INGV-OE (2022a) Etna Bollettino Settimanale Settimana di Riferimento 07/02/2022 - 13/02/2022. Rep. N. 07/2022. Available at <https://www.ct.ingv.it/index.php/monitoraggio-e-sorveglianza/prodotti-del-monitoraggio/bollettini-settimanali-multidisciplinari/601-bollettino-settimanale-sul-monitoraggio-vulcanico-geochimico-e-sismico-del-vulcano-Etna-del-2022-02-15/file>
- INGV-OE (2022b) Etna Bollettino Settimanale Settimana di Riferimento 21/02/2022 - 27/02/2022. Available at <https://www.ct.ingv.it/index.php/monitoraggio-e-sorveglianza/prodotti-del-monitoraggio/bollettini-settimanali-multidisciplinari/605-bollettino-settimanale-sul-monitoraggio-vulcanico-geochimico-e-sismico-del-vulcano-Etna-del-2022-03-01/file>
- Jaupart C, Vergnolle S (1988) Laboratory models of Hawaiian and Strombolian eruptions. *Nature* 331:58–60. <https://doi.org/10.1038/331058a0>
- Jaupart C, Vergnolle S (1989) The generation and collapse of a foam layer at the roof of a basaltic magma chamber. *J Fluid Mech* 203:347–380. <https://doi.org/10.1017/S0022112089001497>
- Kahl M, Chakraborty S, Pompilio M, Costa F (2015) Constraints on the nature and evolution of the magma plumbing system of Mt. Etna volcano (1991–2008) from a combined thermodynamic and kinetic modelling of the compositional record of minerals. *J Petrol* 56:2025–2068. <https://doi.org/10.1093/petrology/egv063>
- La Spina A, Burton M, Salerno GG (2010) Unravelling the processes controlling gas emissions from the central and northeast craters of Mt. Etna *J Volcanol Geotherm Res* 198:368–376. <https://doi.org/10.1016/j.jvolgeores.2010.09.018>
- La Spina A, Burton M, Allard P, Alparone S, Murè F (2015) Open-path FTIR spectroscopy of magma degassing processes during eight lava fountains on Mount Etna. *Earth Planet Sci Lett* 413:123–134. <https://doi.org/10.1016/j.epsl.2014.12.038>
- La Spina A, Arzilli F, Llewellyn EW, Burton MR, Clarke AB, de' Michieli Vitturi M, Polacci M, Hartley ME, Di Genova D, Mader HM (2021) Explosivity of basaltic lava fountains is controlled by magma rheology, ascent rate and outgassing. *Earth Planet Sci Lett* 553:116658. <https://doi.org/10.1016/j.epsl.2020.116658>
- La Spina A, Burton M, Salerno G, Caltabiano T (2023) Insights into magma dynamics at Etna (Sicily) from SO<sub>2</sub> and HCl fluxes during the 2008–2009 eruption. *Geology* 51:419–423. <https://doi.org/10.1130/G50707.1>
- Leibrandt S, Le Pennec JL (2015) Towards fast and routine analyses of volcanic ash morphometry for eruption surveillance applications. *J Volcanol Geotherm Res* 297:11–27. <https://doi.org/10.1016/j.jvolgeores.2015.03.014>
- Lo Castro MD, Andronico D (2008) Operazioni di base per la misura della distribuzione granulometrica di particelle vulcaniche tramite il CAMSIZER. *Rapporti Tecnici INGV* 79:1–35
- Marquardt DW (1963) An algorithm for least-squares estimation of nonlinear parameters. *J Soc Ind Appl Math* 11. <https://doi.org/10.1137/0111030>
- Mastin LG, Guffanti M, Servranckx R, Webley P, Barsotti S, Dean K, Durant A, Ewert JW, Neri A, Rose WI, Schneider D, Lee S, Stunder B, Swanson G, Tupper A, Volentik A, Waythomas CF (2009) A multidisciplinary effort to assign realistic source parameters to models of volcanic ash-cloud transport and dispersion during eruptions. *J Volcanol Geotherm Res* 186(1–2):10–21. <https://doi.org/10.1016/j.jvolgeores.2009.01.008>
- Miwa T, Shimano T, Nishimura T. (2015) Characterization of the luminance and shape of ash particles at Sakurajima volcano, Japan, using CCD camera images. *Bull Volcanol* 77(1). <https://doi.org/10.1007/s00445-014-0886-7>
- Mueller SB, Houghton BF, Swanson DA, Fagents SF, Klawonn M (2018) Intricate episodic growth of a Hawaiian tephra deposit: case study of the 1959 Kīlauea Iki eruption. *Bull Volcanol* 80(73). <https://doi.org/10.1007/s00445-018-1249-6>
- Musa A, Corsaro RA, Higgins O, Jorgenson C, Petrelli M, Caricchi L (2023) The magmatic evolution of South-East Crater (Mt. Etna) during the February–April 2021 sequence of lava fountains from a mineral chemistry perspective. *Bull Volcanol* 85:33. <https://doi.org/10.1007/s00445-023-01643-2>
- Namiki A, Manga M (2008) Transition between fragmentation and permeable outgassing of low viscosity magmas. *J Volcanol Geotherm Res* 169:48–60. <https://doi.org/10.1016/j.jvolgeores.2007.07.020>
- Oppenheimer C, Scaillet B, Woods A, Sutton J, Elias T, Moussallamal Y (2018) Influence of eruptive style on volcanic gas emission chemistry and temperature. *Nat Geosci* 11. <https://doi.org/10.1038/s41561-018-0194-5>
- Pardini F, Corradini S, Costa A, Esposti Ongaro T, Merucci L, Neri A, Stelitano D, de' Michieli Vitturi M (2020) Ensemble-based data assimilation of volcanic ash clouds from satellite observations: application to the 24 December 2018 Mt. Etna. *Explosive Eruption Atmosphere* 11(4):359. <https://doi.org/10.3390/atmos11040359>
- Pardini F, Andronico D, Esposti Ongaro T, Cristaldi A, Neri A (2023) Real-time probabilistic assessment of volcanic hazard for tephra dispersal and fallout at Mt. Etna: the 2021 lava fountain episodes. *Bull Volcanol* 85:6. <https://doi.org/10.1007/s00445-022-01614-z>
- Parfitt EA (2004) A discussion of the mechanisms of explosive basaltic eruptions. *J Volcanol Geotherm Res* 134(1–2):77–107. <https://doi.org/10.1016/j.jvolgeores.2004.01.002>
- Parfitt EA, Wilson L (1995) Explosive volcanic eruptions: IX. The transition between Hawaiian-style lava fountaining and Strombolian explosive activity. *Geophys J Int* 121:226–232. <https://doi.org/10.1111/j.1365-246X.1995.tb03523.x>
- Pichavant M, Di Carlo I, Pompilio M, le Gall N (2022) Timescales and mechanisms of paroxysm initiation at Stromboli volcano, Aeolian Islands, Italy *Bullet Volcanol*. <https://doi.org/10.1007/s00445-022-01545-9>
- Pioli L, Bonadonna C, Azzopardi BJ, Phillips JC, Ripepe M (2012) Experimental constraints on the outgassing dynamics of basaltic magmas. *J Geophys Res Solid Earth* 117:B3. <https://doi.org/10.1029/2011JB008392>
- Polacci M, Corsaro RA, Andronico D (2006) Coupled textural and compositional characterization of basaltic scoria: insights into the transition from Strombolian to fire fountain activity at Mount Etna, Italy. *Geology* 34:201–204. <https://doi.org/10.1130/G22318.1>
- Polacci M, Andronico D, de' Michieli Vitturi M, Taddeucci J, Cristaldi A (2019) Mechanisms of ash generation at basaltic volcanoes:

- the case of Mount Etna, Italy. *Front Earth Sci* 7:193. <https://doi.org/10.3389/feart.2019.00193>
- Pompilio M, Bertagnini A, Del Carlo P, Di Roberto A (2017) Magma dynamics within a basaltic conduit revealed by textural and compositional features of erupted ash: the December 2015 Mt. Etna Paroxysms. *Sci Rep* 7 <https://doi.org/10.1038/s41598-017-05065-x>
- Porritt LA, Russell JK, Quane SL (2012) Pele's tears and spheres: examples from Kīlauea Iki. *Earth Planet Sci Lett* 333–334:171–180. <https://doi.org/10.1016/j.epsl.2012.03.031>
- Powers JG, Klemp JB, Skamarock WC, Davis CA, Dudhia J, Gill David O, Coen JL, Gochis DJ, Ahmadov R, Peckham SE, Grell GA, Michalakes J, Trahan S, Benjamin SG, Alexander CR, Dimego GJ, Wang W, Schwartz CS, Romine GS, Liu X, Snyder C, Chen F, Barlage MJ, Yu W, Barlage Michael J, Duda MG (2017) The weather research and forecasting model: overview, system efforts, and future directions. *Bull Am Meteorol Soc* 98(8):1717–1737 (<https://journals.ametsoc.org/view/journals/bams/98/8/bams-d-15-00308.1.xml>)
- Proietti C, De Beni E, Cantarero M, Ricci T, Ganci G (2023) Provision of rapidly mapping and volcanological parameters: quantification of the 2021 Etna lava flows through the integration of multiple remote sensing techniques. *Bull Volcanol* 85:58. <https://doi.org/10.1007/s00445-023-01673-w>
- Pyle DM (1989) The thickness, volume and grain size of tephra fall deposits. *Bull Volcanol* 51:1–15. <https://doi.org/10.1007/BF01086757>
- Riley CM, Rose WI, Bluth GJS (2003) Quantitative shape measurements of distal volcanic ash. *J Geophys Res Sol Ea* 108(B10). <https://doi.org/10.1029/2001jb000818>
- Rodgers CD (2000) Inverse methods for atmospheric sounding. World Scientific Publishing Co. Pte. Ltd. 256 pp. <https://doi.org/10.1142/3171>
- Romero JE, Vera F, Polacci M, Morgavi D, Arzilli F, Alam MA, Bustillos JE, Guevara A, Johnson JB, Palma JL, Burton M, Cuenca E, Keller W (2018) Tephra from the March 2015 sustained column related to explosive lava fountain activity at Volcán Villarrica (Chile). *Front Earth Sci* 6:98. <https://doi.org/10.3389/feart.2018.00098>
- Rothman LS, Rinsland CP, Goldman A, Massie ST, Edwards DP, Flaud J-M, Perrin A, Camy-Peyret C, Dana V, Mandin J-Y, Schroeder J, Mccann A, Gamache RR, Wattson RB, Yoshino K, Chance KV, Jucks KW, Lr Brown, Nemtchinov V, Varanasi P (1998) The HITRAN molecular spectroscopic database and HAWKS (HITRAN Atmospheric Workstation): 1996 edition. *J Quant Spectrosc Radiat Transf* 60:665–710. [https://doi.org/10.1016/S0022-4073\(98\)00078-8](https://doi.org/10.1016/S0022-4073(98)00078-8)
- Schneider CA, Rasband WS, Eliceiri KW (2012) NIH image to ImageJ: 25 years of image analysis. *Nat Methods* 9:671–675. <https://doi.org/10.1038/nmeth.2089>
- Scollo S, Coltelli M, Bonadonna C, Del Carlo P (2013) Tephra hazard assessment at Mt. Etna (Italy). *Nat Hazards Earth Syst Sci* 13(12):3221–3233. <https://doi.org/10.5194/nhess-13-3221-2013>
- Scollo S, Prestifilippo M, Bonadonna C, Cioni R, Corradini S, Degruyter W, Rossi E, Silvestri M, Biale E, Carparelli G (2019) Near-real-time tephra fallout assessment at Mt. Etna, Italy. *Remote Sens* 11(24). <https://doi.org/10.3390/rs11242987>
- Seyfried R, Freundt A (2000) Experiments on conduit flow and eruption behavior of basaltic volcanic eruptions. *J Geophys Res Solid Earth* 105:23727–23740. <https://doi.org/10.1029/2000JB900096>
- Shea T, Houghton BF, Gurioli L, Cashman KV, Hammer JE, Hobden BJ (2010) Textural studies of vesicles in volcanic rocks: an integrated methodology. *J Volcanol Geotherm Res* 190(3–4):271–289. <https://doi.org/10.1016/j.jvolgeores.2009.12.003>
- Spanu A, de' Michieli Vitturi M, Barsotti S (2016) Reconstructing eruptive source parameters from tephra deposit: a numerical study of medium-sized explosive eruptions at Etna volcano. *Bull Volcanol* 78:1–19. <https://doi.org/10.1007/s00445-016-1051-2>
- Spilliaert N, Allard P, Métrich N, Sobolev AV (2006) Melt inclusion record of the conditions of ascent, degassing, and extrusion of volatile-rich alkali basalt during the powerful 2002 flank eruption of Mount Etna (Italy). *J Geophys Res Solid Earth* 111:B04203. <https://doi.org/10.1029/2005JB003934>
- Stein A, Draxler RR, Rolph GD, Stunder BJ, Cohen M, Ngan F (2015) NOAA's HYSPLIT atmospheric transport and dispersion modeling system. *Bull Am Meteorol Soc* 96(12):2059–2077. <https://doi.org/10.1175/BAMS-D-14-00110.1>
- Stovall WK, Houghton BF, Gonnermann H, Fagents SA, Swanson DA (2011) Eruption dynamics of Hawaiian-style fountains: the case study of episode 1 of the Kīlauea Iki 1959 eruption. *Bull Volcanol* 73(5):511–529. <https://doi.org/10.1007/s00445-010-0426-z>
- Stovall WK, Houghton BF, Hammer JE, Fagents SA, Swanson DA (2012) Vesiculation of high fountaining Hawaiian eruptions: episodes 15 and 16 of 1959 Kīlauea Iki. *Bull Volcanol* 74:441–455. <https://doi.org/10.1007/s00445-011-0531-7>
- Swanson DA, Duffield WA, Jackson DB, Peterson DW (1979) Chronological narrative of the 1969–71 Mauna Ulu eruption of Kīlauea volcano Hawaii. *US Geol Surv Prof Pap* 1056:1–55
- Taddeucci J, Pompilio M, Scarlato P (2002) Monitoring the explosive activity of the July–August 2001 eruption of Mt. Etna (Italy) by ash characterization. *Geophys Res Lett* 29:1029–1032. <https://doi.org/10.1029/2001GL014372>
- Taddeucci J, Pompilio M, Scarlato P (2004) Conduit processes during the July–August 2001 explosive activity of Mt. Etna (Italy): inferences from glass chemistry and crystal size distribution of ash particles. *J Volcanol Geotherm Res* 137:33–54
- Tadini A, Gouhier M, de' Michieli Vitturi FM, Pardini F (2022) Particle sedimentation in numerical modelling: a case study from the Puyehue-Cordón Caulle 2011 eruption with the PLUME-MoM/HYSPLIT models. *Atmosphere* 13(5):84. <https://doi.org/10.3390/atmos13050784>
- Thivet S, Gurioli L, Di Muro A (2020a) Basaltic dyke eruptions at Piton de La Fournaise: characterization of the eruptive products with implications for reservoir conditions, conduit processes and eruptive dynamics. *Contrib Mineral Petrol* 175:26. <https://doi.org/10.1007/s00410-020-1664-5>
- Thivet S, Gurioli L, Di Muro A, Derrien A, Ferrazzini V, Gouhier M, Coppola D, Galle B, Arellano S (2020b) Evidences of plug pressurization enhancing magma fragmentation during the September 2016 basaltic eruption at Piton de la Fournaise (La Réunion Island, France). *Geochem Geophys Geosyst* 21:e201
- Thivet S, Gurioli L, Di Muro A, Eychenne J, Besson P, Nedelec JM (2020c) Variability of ash deposits at Piton de la Fournaise (La Reunion Island): insights into fragmentation processes at basaltic shield volcanoes. *Bull Volcanol* 82:63. <https://doi.org/10.1007/s00445-020-01398-0>
- Tomašek I, Damby DE, Andronico D, Baxter PJ, Boonen I, Claeys P, Denison MS, Horwell CJ, Kervyn M, Kueppers U, Romanias MN, Elskens M (2021) Assessing the biological reactivity of organic compounds on volcanic ash: implications for human health hazard. *Bull Volcanol* 83:30. <https://doi.org/10.1007/s00445-021-01453-4>
- Toramaru A (1995) Numerical study of nucleation and growth of bubbles in viscous magmas. *J Geophys Res* 100:1913–1931
- Toramaru A (2006) BND (bubble number density) decompression rate meter for explosive volcanic eruptions. *J Volcanol Geotherm Res* 154:303–316

- Vergnolle S (1996) Bubble size distribution in magma chambers and dynamics of basaltic eruptions. *Earth Planet Sci Lett* 140:269–279. [https://doi.org/10.1016/0012-821X\(96\)00042-8](https://doi.org/10.1016/0012-821X(96)00042-8)
- Vergnolle S (2008) From the sound waves and the height of fire fountains to the depth of a magma reservoir at Etna (Italy) and Kilauea (USA) volcanoes. *Geol Soc London* in “Fluid motion in volcanic conduits: a source of seismic and acoustic signals” 307:125–146
- Vergnolle S, Gaudemer Y (2012) Decadal evolution of a degassing magma reservoir unravelled from fire fountains produced at Etna (Italy) between 1989 and 2001. *Bull Volcanol* 74:725–742
- Vergnolle S, Jaupart C (1986) Separated two-phase flow and basaltic eruptions. *J Geophys Res* 91(B3):12842–12860
- Vergnolle S, Jaupart C (1990) Dynamics of degassing at Kilauea volcano. *Hawaii J Geophys Res* 95(B3):2793–2809. <https://doi.org/10.1029/JB095iB03p02793>
- Webster HN, Devenish BJ, Mastin LG, Thomson DJ, Van Eaton AR (2020) Operational modelling of umbrella cloud growth in a Lagrangian volcanic ash transport and dispersion model. *Atmosphere*, 11(2) <https://doi.org/10.3390/atmos11020200>
- White JDL, Houghton BF (2006) Primary volcaniclastic rocks. *Geology* 34(8):677–680. <https://doi.org/10.1130/G22346.1>
- Zimmerman D, Pavlik C, Ruggles A, Armstrong MP (1999) An experimental comparison of ordinary and universal kriging and inverse distance weighting. *Math Geol* 31(4):375–390. <https://doi.org/10.1023/A:1007586507433>